Energy & Environmental Science

Accepted Manuscript

ROYAL SOCIETY OF CHEMISTRY

www.rsc.org/ees

Energy & Environmental Science

Dynamic Article Links ►

Review

Cite this: DOI: 10.1039/c0xx00000x

www.rsc.org/xxxxxx

Hierarchical Electrospun Nanofibers for Energy harvesting, production and Environmental remediation

Palaniswamy Suresh Kumar,[ab*] Jayaraman Sundaramurthy,[ab*] Sundarrajan Subramanian,[c] Veluru Jagadeesh Babu,[d] Gurdev Singh,[b] Suleyman I. Allakhverdiev,[ef] Seeram Ramakrishna[ac*]

Received (in XXX, XXX) Xth XXXXXXXXX 20XX, Accepted Xth XXXXXXXXX 20XX
DOI: 10.1039/b000000x

As the energy demand is rapidly growing worldwide against the energy supply, there is an impulse need to develop alternative energy-harvesting technologies to sustain the energy economic growth. Due to the unique optical and electrical properties, one-dimensional (1D) electrospun nanostructured materials are attractive for construction of active energy harvesting devices such as photovoltaic, photocatalysis, hydrogen energy generation, and fuel cells. 1D nanostructures produced from electrospinning possess high chemical reactivity, high surface area, low density, improved light absorption and dye adsorption compared to their bulk counterparts. So, the focus has been devoted to synthesize 1D nanostructured fibers made from metal oxides, composite, dopant and surface modification. Further, fine tuning the NFs facilitates in achieving fast charge transfer and efficient charge separation for the improved light absorption in photocatalytic and photovoltaic properties. The recent trend to explore these electrospun nanostructures are promising in-terms of reduced cost and enhancement in efficiency compared to conventional materials. This review article presents the synthesis of 1D nanostructured fibers from electrospinning and their applications in photovoltaic, photocatalysis, hydrogen energy harvesting and fuel cells. The current challenges and future perspectives of electrospun nanomaterials are also reviewed.

1. Introduction

In recent years, the world has been facing enormous challenges in energy demands, depleting power sources, and environmental pollutions. The demand for energy is rapidly increasing. The total primary energy production of the world was 1.02 x 10^5 TW h in 1990 and 1.49 x 10^5 TW h in 2010 and extrapolated statistics indicate figures of around 1.81 x 10^5 TW h in 2020, 2.11x 10^5 TW h in 2030 and 2.25 x 10^5 TW h in 2035, with an average annual percentage change of 1.6%[1-4]. In last few decades, the increasing concern about global warming due to emissions of greenhouse gases has received attention from governments across the globe to alter the energy policies and strategies. Hence, it's important to reduce our dependence on fossil fuels by augmenting it with supplies from cleaner, renewable sources of energy. In order to overcome these challenges, researchers have worked to create new functional nanomaterials and technology. Although these emerging energy technologies signify importance towards existing energy demands, new breakthroughs are needed to improve their performance. The nanostructure materials have received extensive attentions in recent years which possess high surface areas significantly larger than that of bulk materials. This nanosize improves the behaviour of electrons transporting in nanostructures in view of a limit to the electron mean free path due to quantum confinement effect[5-7]. Hierarchical nanostructure materials have unique functional properties and fascinating applications in photonics devices (light emitting diode, UV detectors), energy (dye-sensitized solar cells (DSSCs), batteries, fuel cell, water-splitting[8-11], environmental (coatings, photocatalysis, air and water filtration)[12-15] and biological domains (drug delivery, tissue engineering)[16, 17]. So far, various methods such as precipitation[18], solution[19], hydrothermal[20], template synthesis[21], sol-gel[22], successive ionic layer adsorption and reaction process[23] have been adopted to synthesis different form of nanostructures such as nanorods, nanotubes, nanowires, nanoflowers and etc[24-26]. Among these methods, electrospinning is one of the simplest and most effective technologies for scaling-up wide range of electrospun nanomaterials towards industrial production. In recent years, great progress has been made in electrospinning and with controlled growth of novel electrospun NFs which shown great potential in different fields such as energy storage[27], sensor[28], water filtration[29] and biomedicine/tissue engineering[30]. Notwithstanding the economic

recession, the value of the global nanofiber (NF) market increased from $43.2 million in 2006 to $101 million in 2010, and is projected to reach 2.2 billion by 2020[31, 32]. The categorization in Fig. 1 is simplified illustration of future and ongoing research works on hierarchical electrospun fibers for energy and environmental remediation's. This review combines knowledge to stimulate recent development in electrospinning and demonstrate the potential of NFs with improved functionality, versatility of hierarchical surface morphologies towards energy harvesting, production and environmental applications and finally the future perspective on the electrospun fibers.

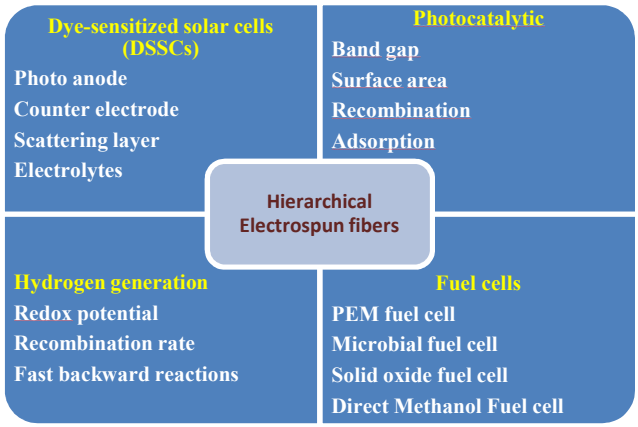

Fig. 1 Overview and simplified illustration table on future and ongoing research works on hierarchical electrospun fibers for energy and environmental remediation.

2. Electrospinning

Electrospinning is an effective and simple method to fabricate nanomaterials with diameters ranging from tens of nanometers up to micrometers. The electrospinning technique has been developed in1934 for the synthesis of 1D material and demonstrated that a rich variety of materials can be electrospun to form uniform 1D material, such as polymers, inorganic and hybrid (organic/inorganic) composites. Ceramic NFs are synthesized from electrospun organometallic NFs by heating in an oxidizing atmosphere. Metal NFs or nanowires were produced by heating the NF that contained metal atoms in a reducing atmosphere. Hydrocarbon NFs such as polyacrylonitrile were converted to carbon NFs by low temperature oxidation followed by heating in an inert atmosphere.

Electrospinning generate ultrathin fibers from few nm to few µm with wide variety of materials that include metal oxide/ceramics[33-36] such as CuO, Fe_2O_3, TiO_2 and NiO, mixed metal oxides such as $NiFe_2O_4$, $TiNb_2O_7$, and $LiMn_2O_4$[37-39],composites[40-42] such as PVA/TiO_2, Carbon/SnO_2, Graphene/TiO_2, Nylon-6/gelatin, collagen/hydroxyapatite, and polymers[43,44] such as polyvinylaclohol (PVA), polyacrylonitrile (PAN), polyvinylidene fluoride (PVDF), polyvinylpyrrolidone (PVP), polyethylene glycol (PEG), polystyrene (PS) and carbon based materials. The electrospinning with controlled calcinations can provide a simple route to produce hierarchical nanostructures that are difficult to fabricate using other methods.

2.1 Basic principles in Electrospinning

Electrospinning technique is a unique approach using electrostatic forces to produce fine fibers from polymer solutions or melts and the fibers thus produced have a thinner diameter (from nanometer to micrometer) with larger surface area than those obtained from conventional spinning processes. Various techniques such as electrostatic precipitators and pesticide sprayers work similarly to the electrospinning process and this process, mainly based on the principle that strong mutual electrical repulsive forces overcome weaker forces of surface tension in the charged polymer liquid. Basically, an electrospinning system consists of three major components: a high voltage power supply, a spinneret and a grounded collecting plate (usually a metal screen, plate, or rotating mandrel) and it utilizes a high voltage source to inject charge of a certain polarity into a polymer solution or melt, which is then accelerated towards a collector of opposite polarity. Typically, electrospinning technique involves the use of a high voltage electrostatic potential (~5–30 kV), field to charge the surface of polymer solution droplet and thus to induce the ejection of a liquid jet through a spinneret (single, multi-spinneret and co-axial)[32].

In a typical process, an electrical potential is applied between a droplet of a polymer solution or melt, held at the end of a capillary tube and a grounded target. When the applied electric field overcomes the surface tension of the droplet, a charged jet of polymer solution is ejected from the tip of the needle. The jet exhibits bending instabilities caused by repulsive forces between the carried charges. The jet extends through spiralling loops, as the loops diameter increase when the jet grows longer and thinner and then it solidifies or collects on the target. These NFs have unique characteristics such as high surface-to-volume ratio, ability to produce highly porous fibrous with excellent pore interconnectivity, controllability in fiber diameter, surface morphology and fibrous structure[43, 45, 46]. Electrospinning of NFs with wide varieties of morphologies including dense[47], hollow[48], and porous[49] structures for specific applications have been achieved by changing the process parameters such as electric potential, flow rate, polymer concentration, distance between the capillary and collection screen and ambient parameters[50]. Fig. 2(a) shows the typical electrospinning set-ups for random-aligned NF synthesis.

2.2 Coaxial Electrospinning

The important breakthrough in electrospinning is coaxial electrospinning in which a spinneret consisting of two coaxial capillaries is used with two viscous fluids (or non-viscous liquid as core and viscous fluid as shell) form a core/shell compound jet in an electric field and then solidify to form core/shell fibers. Compared with other methods, it is very attractive and simple, effective top-down way to prepare core/shell ultrathin fibers with lengths of up to several centimeters on a large scale. It has been reported that polymer, organic, inorganic, and hybrid core/shell and hollow materials have been fabricated by this facile method. Among all parameters, the immiscibility of core and sheath liquids is most crucial to the formation of continuous and uniform hollow fibers. Hollow structures were observed after polymers had been removed by solvent extraction or by calcination at an elevated temperature, although the core liquid was sufficiently viscous to be electrospun as fibers with diameters as thin as a few hundred nanometers[51]. Fig. 2(b) shows the typical electrospinning

set-up for core-shell NFs synthesis.

The following parameters and processing variables affect the electrospinning process: (i) system parameters such as molecular weight, molecular weight distribution and architecture of the polymers (like branched, linear, etc), and polymer solution properties (viscosity, conductivity, dielectric constant, surface tension, and charge carried by the spinning jet) and (ii) processing parameters such as electric potential, flow rate and concentration, distance between the capillary and collection screen, ambient parameters (temperature, humidity and air velocity in the chamber) and finally motion of the target screen. For instance, the polymer solution must have a concentration high enough to cause polymer entanglements yet not so high that the viscosity prevents polymer motion induced by the electric field. The solution must have surface tension low enough with charge density high enough and viscosity high enough to prevent the jet from collapsing into droplets before the solvent has evaporated. Morphological effect can occur upon decreasing the distance between the syringe needle and substrate. Increasing the distance or decreasing the electrical field decreases the bead density, regardless the concentration of polymer in solution. Applied fields can moreover influence the morphology in periodic ways, creating a variety of new shapes on the surface. In addition to creating circular NFs, electrospinning of a polymer solution can produce thin fibers with a varieties of cross-sectional shapes[52].

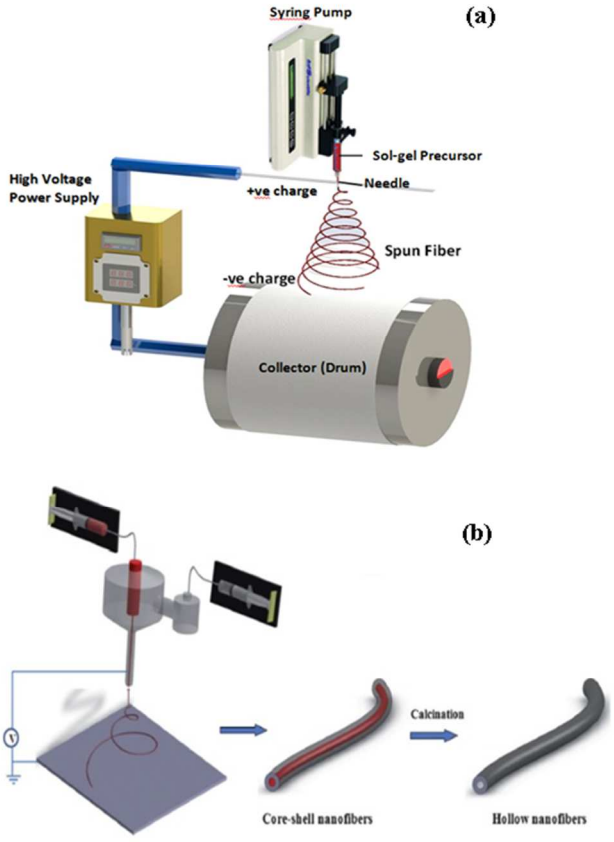

Fig. 2 Different types of electrospinning set-up for fiber production: (a) random/aligned fibers (b) core-shell/hollow NFs[48].

2.3 Influencing parameters on the electrospinning process

(a) Viscosity

Solution surface tension and viscosity play important roles in determining the range of concentrations from which continuous fibers can be obtained in electrospinning. Viscosity is a function of the concentration of solution and molecular weight of the polymer. When the viscosity of the solution is too low, electrospraying may occur and polymer particles are formed instead of fibers. At a lower viscosity, where usually the polymer chain entanglements are lower, which leads to beaded fibers instead of smooth fibers. Therefore, factors that affect viscosity of the solution will also affect the electrospinning process and the resultant fibers. The higher viscosity solutions proved extremely difficult to force through the syringe needle, making the control of solution flow rate to the tip unstable.

(b) Applied electric field (V)

The electric field are varied over a range, for stable electrospinning, however when the point to collector distance was changed to 5cm, stable electrospinning only occurs at an electric field of 1-2kV/cm. In electrospinning, the charge transport due to applied voltage is mainly due to flow of the solution jet towards the collector and increase or decrease of current is attributed to the mass flow of solution from the spinneret tip. Increase in applied voltage causes a change in the shape of jet initiating point which alters the structure and morphology of the fibers.

(c) Spinneret collector and feed rate

Different spinneret collectors such as foils, metals and rotating drums have been utilized by numerous researchers. The typical electrode used widely is aluminium foil, due to its inexpensive price, availability, and ease of changing for the analysis of many samples. The foil is connected to a ground electrode to provide a path for the current to travel. Generally, rotating drums are used to produce NFs with uniform thickness and whenever reproducible results are the primarily desired. The flow rate of the solution from the syringe is an important process parameter as it influences the jet velocity and the material transfer rate. With a lower solution feeding rate, smaller the fibers with spindle-like beads are formed and vice versa

2.4 Advantages of electrospinning

Electrospinning is a simple and elegant method for NF production from organic and inorganic materials. This technique has brought up significant attention since the 1990s, due to its versatility and economic competitiveness at laboratory scales of fiber production. It can be used for the tuneable nanostructures and properties for the wide range of applications[43, 53-57]. These unique and fascinating properties of these electrospun nanostructure materials with well-defined geometrical shapes have triggered tremendous motivation among scientists for its multifaceted applications such as DSSC, dye degradation, water-splitting and fuel cell. Fig. 3(a) illustrates the growing research on electrospun materials annually and (b) corresponding research articles published on the use of electrospun NF in energy domains (DSSCs, photocatalytic, hydrogen generation and fuel cells).

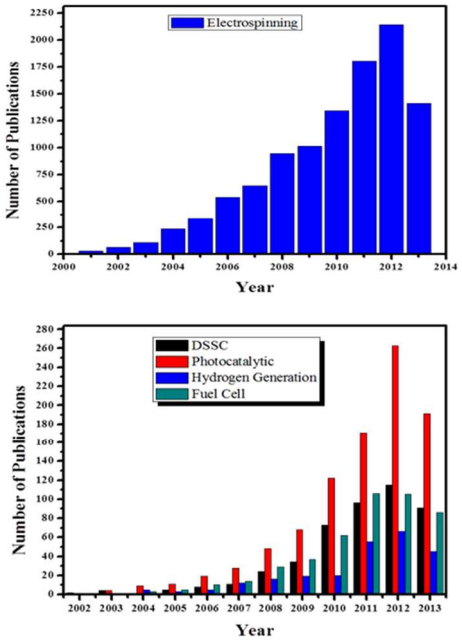

Fig.3 Comparison of (a) number of research publications produced within last ten years (2000 to 2013) using electrospinning and (b) research articles published on using electrospun NFs in energy domain (DSSCs, photocatalytic, hydrogen generation and fuel cells).

3. Electrospun fiber based Dye-Sensitized Solar Cells (DSSCs)

Solar energy is abundant as more sun light strikes the earth in a day than the total energy consumption of the world in a year. Despite the vast availability, the energy produced from solar remains only 0.01% of the total energy demands[3, 58, 59]. Over the past five years, solar PV has averaged an annual growth rate of over 50% and present trend of using photovoltaic for electricity generation is increasing rapidly from 1.5 GW to 67 GW from 2000 to the end of 2011 all over the world[4]. Photovoltaic (PV) technology has advanced rapidly both in the materials technology and the device architectures. DSSCs have been widely recognized as a promising alternative to conventional silicon cells since they were reported by O'Regan and Grätzel in 1991[60]. DSSCs are sometimes included in the category of organic solar cells because of the organic nature of the sensitizer dye. However, the third generation solar cells have a lot of attractive features superior to the first and second generation solar cells, for example, the compatibility with flexible substrates and low cost of materials and manufacturing. Of the solar cells, fabrication of DSSCs is the simplest and economical. Until recently, the highest DSSCs power conversion efficiency that has been achieved is more than 12%, which is lower than that of bulk silicon solar cells[61]. However, it is difficult to predict the determining factors to enhance its efficiency, which is still a crucial issue and plenty of research has been carried out to improve the performance of DSSCs by various methods[62, 63].

A typical DSSC device is structurally composed of a photoactive n-type semiconductor working electrode (photo anode), a counter electrode made up of either metal or semiconductor (photocathode), and an electrolyte. DSSC cell consists of a photo electrode mesoporous layer (commonly, TiO_2) of a suitable metal oxide on a conducting glass (fluorine-doped tin oxide, F-SnO_2). The surface of the oxide layer is chemisorbed with a layer of an organic dye, which acts as a sensitizer. The cell is made complete by sealing against a counter electrode in the presence of an electrolyte and the electrolyte helps in regenerating the dye. Upon shining light, the excited electrons of the dye are transferred to the conduction band (CB) of the oxide layer and are transported out through an external circuit[63-66]. The detailed schematic diagram of electrospun based DSSCs is shown in Fig. 4.Electrospun NF (TiO_2, ZnO, CuO) based DSSCs have received considerable attention from the academic community and industry for their ease of production, high efficiency and environmental-friendliness with abundant, inexpensive materials.

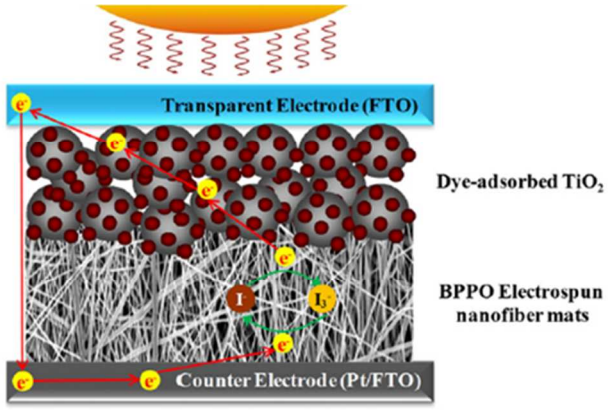

Fig. 4 Schematic diagram of electrospun NF based DSSCs[67].

Highly ordered nanostructures of TiO_2, and other wide band gap semiconductors are promising alternatives to the mesoporous NP thin films that are currently used for DSSCs. However, up to now, most successful DSSCs are based on TiO_2 nanostructure materials owing to their integrated advantage in porosity, dye adsorption, charge transfer, and electron transport[68]. Hierarchical electrospun TiO_2 NF with tuneable diameters are one of the available 1D materials which has great potential for use in the fabrication of DSSC with several advantages over other methods; large-area applicability, environmental friendliness and room temperature process. *Lee et al*. fabricated DSSCs with high energy conversion efficiencies using TiO_2electrospun nanorods[69]. The electron diffusion coefficient of post treated nanorod was ~51% higher than that of an untreated one, leading to a charge collection efficiency that was 19% higher at an incident photon flux of $8.1 \times 10^{16} cm^{-2} s^{-1}$. The efficiency of nanorod-based DSSCs with device thickness of 14μm are found to be 9.52% with V_{oc} =761 mV, J_{sc} = 17.6 mA cm^{-2}, and fill factor =70.0%. *Lin et al*. reported a series of 1D mesoporous anatase TiO_2NFs (TNFx, x = 0−3 in wt%) with 0−3wt% of room-temperature ionic liquid (RTIL) as the mesopore formation template[70]. The DSSC fabricated with TNF1 showed the largest improvement (~50.4%) in energy conversion efficiency (5.64%) over that with TNF0 electrospun without RTIL (3.75%). These enhancement of the energy conversion efficiency were mainly attributed to the more efficient light harvesting caused by the larger amount of dye adsorbed and faster electron transport in the TNFx-based (x > 0) photoanodes. *Li et al.* fabricated highly transparent nanocrystalline TiO_2 films by electrospinning of NFs based on a transmutation process[71]. The electrospun NF films possessed rich bulk oxygen vacancies (BOVs, PL band at 621-640 nm) when

measured by using photoluminescence (PL) spectroscopy. The double-layer cell yielded a high efficiency of 6.01%, which had been increased by 14% as compared with that obtained from a 10 mm thick P25 film. *Song et al.* developed single crystalline TiO_2 nanorods electrodes from electrospun fibers after calcination[72]. This electrode provided an efficient photocurrent generation in a quasi-solid-state dye-sensitized solar cell with overall conversion efficiency of 6.2%. *Kumar et al*. reported highly crystalline hierarchical TiO_2 nanostructures of morphology ranging from one-dimensional regular fibers, hollow tubes, porous rods and spindles through electrospun TiO_2/composite fibers[73]. XRD analysis confirmed the phase transformations from anatase to rutile with crystallite size variation from 11 nm to 36 nm, which was observed upon changing the annealing temperature. At 500°C, surface morphology showed a highly porous rods structure with average length of 1.5 mm and a diameter of 150 nm as shown in Fig. 5 (a-b). A higher conversion efficiency (η) of 4.56% with a short circuit current (J_{sc}) of 8.61 mA cm^{-2} was observed for ordered porous anatase TiO_2nanorods with higher surface area of 75.74 $m^2 g^{-1}$.

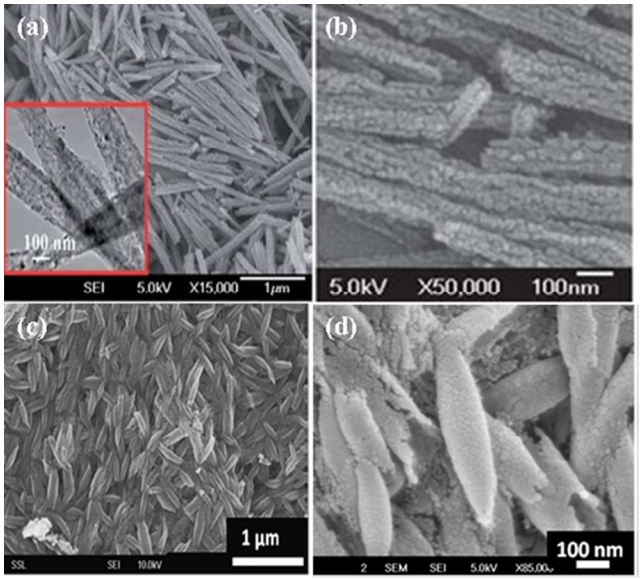

Fig. 5 (a-b) Low and high resolution FESEM image of electrospun porous TiO_2 nanorods prepared at 500°C and insert shows the corresponding TEM images[73]. and (c-d) sintered TiO_2–CNT nanocomposite and TiO_2–CNT (0.2 wt%) nanocomposite revealing the rice grain-shaped morphology[74].

Anjusree et al. reported morphology control of the electrospun TiO_2 depends on the chemical interactions between the polymer and the TiO_2 during the sintering process[75]. The change in polymer mixture from polyvinyl pyrrolidone (PVP) to polyvinyl acetate (PVAc) resulted in the varied morphology of TiO_2 from continuous fibre to rice-shaped to leaf-shaped with device efficiency of 4.5% under 0.5 AM with current density of 5.7 mA cm^{-2},an open circuit voltage of 0.65 V and with a fill factor of 59.4%. *Yang et al.* reported an innovative bilayer TiO_2 NFs photoanode with significantly improved performance of DSSCs[76]. In the case of bilayer photoanode DSSCs with thickness 8.9 μm, they observed significant increase in the photocurrent density and obtain a highest PCE of 8.40% and the corresponding J_{sc} is 22.5 mA cm^{-2}, while the performance of the single-layer photoanode with approximately the same thickness (9.2 μm) had a PCE of just 7.14% and J_{sc} of 20.1 mA cm^{-2}. The conversion efficiency of the bilayer photoanode DSSC device had improved more than 20% compared with the single-layer photo anode devices. *Nair et al.* reported a simple recipe for the fabrication of electrospun TiO_2 nanorod-based efficient dye-sensitized solar cell using a Pechini-type sol[77]. The Pechini-type sol of TiO_2 NFs produced a highly porous and compact layer of TiO_2 upon doctor- blading and sintering without the need for an adhesion and scattering layers or $TiCl_4$ treatment. The best NF DSSCs with an area of ~0.28 cm^2 showed an efficiency of ~4.2% and an incident photon-to-electron conversion efficiency (IPCE) of ~50%and similarly they also demonstrated titanate-derived high surface area TiO_2 observed ~ 50% higher efficiency than that of the fiber/rice grain-shaped anatase TiO_2 (4.63% and 4.49%)[78].

Krysova et al. also reported porous structured electrospun TiO_2 NF with diameters 100–280 nm and surface areas 9–100 m^2/g and the NF efficiencies were investigated by incorporating with mesoporous TiO_2 films[79]. Incorporation of NFs into the mesoporous film resulted in a decrease in dye N719 adsorption but at the same time increased the roughness factor. The preparation of thick mesoporous TiO_2 NF electrodes showed improved solar efficiency of 5.51% which outperformed the pure mesoporous film efficiency (4.96%). *Peining et al.* reported TiO_2–CNT nanocomposites with a novel single crystalline rice-grains nanostructure which were synthesized by cost effective electrospinning followed by subsequent high temperature sintering[74]. They observed at very low CNT loadings (0.1–0.3 wt% of TiO_2), the rice grain shape remains unchanged while at high CNT concentrations (8wt%), the morphology distorted with CNTs sticking out of the rice-grain shape (Fig. 5(c)) 0.2 wt% optimum concentration of CNTs - TiO_2 matrix (Fig. 5(d)) showed the best performance in DSSCs of 32% enhancement in energy conversion efficiency. Similarly, *Peining et al*. fabricated electrospun one-dimensional TiO_2−graphene nanocomposite (TGC) with an average dimension of around ~450 nm in length and ~150 nm in diameter[80]. With the introduction of the graphene into the TiO_2 network, the J_{sc} has been improved from 9.58 to 12.78 mA cm^{-2}. The fill-factor remained at ~62% with enhancement in overall energy conversion efficiency from 4.89 to 6.49%. *Li et. al.* adopted a novel polymer NF/TiO_2 NP composite photoelectrode with high bendability by a spray-assisted electrospinning method[81]. These composite photoelectrodes in plastic DSSCs showed an outstanding mechanical stability for flexible DSSCs even after 1000 bending cycles because crack formation and propagation was effectively suppressed by PVDF NFs and this level of stability was much greater than that of a conventional photoelectrode film consisting of only TiO_2. *Zhang et al.* successfully synthesized hollow mesoporous TiO_2 NFs by co-axial electrospinning of a titanium tetraisopropoxide (TTIP) solution with two immiscible polymers; poly (ethylene oxide) (PEO) and PVP using a core–shell spinneret[82]. The hollow mesoporous TiO_2 NFs were found to have an average diameter of 130 nm with a high surface area of 118 $m^2 g^{-1}$.The solar-to-current conversion efficiency (η) and short circuit current (J_{sc}) were measured as 5.6% and 10.38 mA cm^{-2} respectively, which were higher than those of DSSC made using regular TiO_2 NFs

under identical conditions (η = 4.2%, J_{sc} = 8.99 mA cm^{-2}).The improvements in the conversion efficiency were mainly attributed to the higher surface area and mesoporous TiO_2 nanostructure. *Jin et al.* developed electropsun TiO_2–ZrO_2 fiber composite electrodes by sol–gel and electrospinning techniques[83]. These ZrO_2 fibers intoTiO_2 electrodes provided good dye loading and an effective electron pathway to increase the charge transfer in theTiO_2/electrolyte interface over conventional TiO_2 electrode. Energy conversion efficiency of DSSCs of this composite electrode was 6.2%, with an increase of 26.5% than pure TiO_2 electrode (4.9%). *Du et al.* reported a novel TiO_2/ZnO core–sheath NFs film fabricated through an extraordinary coaxial electrospinning technique as shown in Fig. 6 (middle)[84]. The surface morphology of randomly oriented PVAc/TTIP/$Zn(CH_3COO)_2$ composite fibers had smooth surfaces, the diameters were around 200 nm and after calcination the diameter was reduced by ~25% to ca. 150 nm due to the removal of DMF and PVAc (Fig. 6 (a-d)).The photo-conversion efficiency of 5.17%were observed for TiO_2/ZnO NFs film based photo anode material and which was approximately 16% larger than the bare TiO_2 NFs based DSSCs. The increase in J_{sc} was ascribed to the improved light harvesting efficiency and electron collection efficiency.

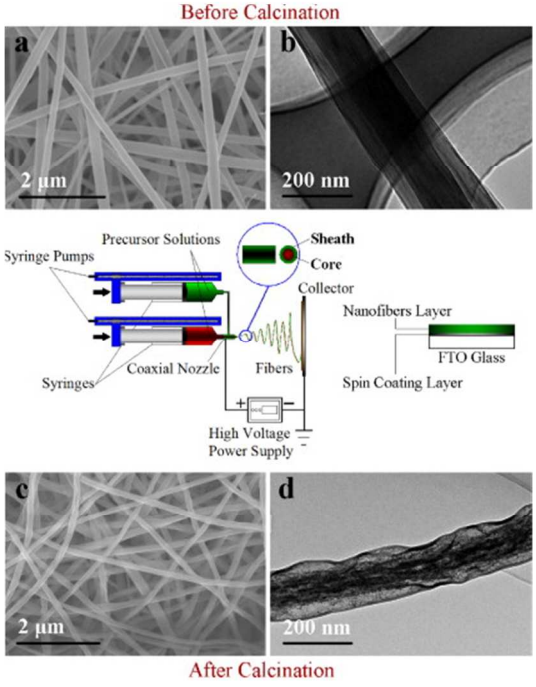

Fig. 6 FESEM/TEM images of PVAc/TTIP/$Zn(CH_3COO)_2$ composite fibers (a-b) before and (c-d) after calcinations and schematic diagram (middle) of coaxial electrospinning[84].

However, the important drawback of DSSCs using liquid electrolyte was that the lower long-term stability due to the volatility of the electrolyte containing organic solvent. To commercialize, durability is a crucial component. Replacing the liquid electrolytes with solid-state electrolytes (SSE), polymer electrolytes (PE) have been considered as one of the crucial issues in order to fully capitalize on the merits of DSSCs, which has resulted in not only improvement in their mechanical stability and simplifying fabrication processes, but also eliminating the need for hermetic sealing. *Hwang et al.* demonstrated high-performance solid-state DSSCs using hierarchically structured TiO_2 NF electrodes and plastic crystal-based solid-state electrolytes[85]. Fig. 7(a-b) shows the typical spinning setup with TiO_2/polymer composite NFs and high density of nanorods with average length between 150-200 µm were obtained. The solid-state DSSCs using NFs demonstrated improved power conversion efficiency (PCE) compared to conventional TiO_2 NP based DSSCs. The optimized PCE of NF using the PC electrolytes were 6.54, 7.69, and 7.93% at the light intensity of 100, 50, and 30 mW cm^{-2}, respectively, with an increased charge collection efficiency (>40%) (Fig. 7(c)).

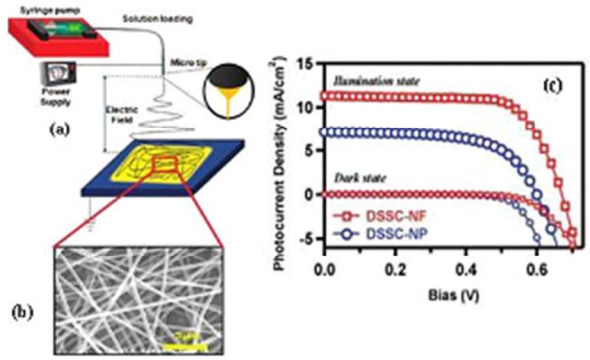

Fig. 7 (a) Schematic description of electrospinning technique to prepare HS-NFs, (b) SEM images of as electrospun TiO_2/polymer composite NFs and (c) J-V curves measured under simulated AM 1.5G light one sun condition[85].

Ahn et al. developed poly (vinylidene fluoride-co-hexafluoropropylene) (e-PVdF-co-HFP) based NFs as polymer gel electrolytes (PGE)[86]. The cells containing electrospun e-PVdF-co-HFP polymer gel electrolyte, with and without doping with the liquid crystal E7 and with a liquid electrolyte were fabricated. Owing to the high ionic conductivity (2.9×10^{-3}) of the E7 when embedded on e-PVdF-co-HFP-PGE, higher values of J_{sc} (14.62 $mAcm^{-2}$) and PCE (6.82%) of the quasi-solid-state DSSCs were achieved. The quasi solid-state DSSC of e-PVdF-co-HFP PGE were found to be ~ 6.35% PCE. *Kim et al.* prepared PVDF-HFPNFs by the electrospinning and applied to the polymer matrix in polymer electrolytes for DSSCs[87]. The ionic conductivity and porosity of the electrospun PVDF-HFP NF films showed 653±50%, $4.53x10^{-3}$S/cm, the diameter and morphology of NFs were around 70±2.3%. The best results of Voc, J_{sc}, FF and Z of the DSSC devices using the electrospun PVDF-HFP NF films were around 0.75 V, 12.3$mAcm^{-2}$, 0.57, and 5.21%. *Sethupathy et al.* reported electrospun fibrous membranes of hybrid composites of polyvinylidene fluoride (PVdF), polyacrylonitrile (PAN) and silicon dioxide (SiO_2) (PVdF-PAN-SiO_2) were prepared at different proportions of SiO_2 (3, 5and 7% w/w)[88]. Photovoltaic performance exhibited an open circuit voltage (V_{oc}) of 0.79 V and a short circuit current 11.6 mA cm^{-2} with efficiency of 5.61%. *Dissanayake et al.* reported NF membrane electrolytes to fabricate quasi-solid state (gel) DSSCs and the performance of these solar cells were compared with DSSCs fabricated with liquid electrolyte and conventional PAN based gel electrolyte (PAN:KI:PC:I2)[89]. DSSC with NF membrane electrolyte of thickness 9.14 µm exhibited highest

light-to-electricity conversion efficiency of 5.2% whereas an identical cell based on corresponding liquid electrolyte showed an efficiency of 5.3%.

The counter electrode (CE) is also an important and expensive component in DSSCs. CE is commonly made of a thin layer of noble-metal platinum catalyst deposited on a transparent conducting oxide (TCO) substrate, such as fluorine-doped tin oxide (FTO) or indium-doped tin oxide (ITO). Most often, Pt are used as a CE in DSSC mainly for two reasons: (a) it acts as a catalyst that helps in the regeneration of I^- from I^-_3, and (b) collection of electrons from the external load to the electrolyte. Even though, Pt is an extremely expensive noble metal, it is used often for its electrocatalytic activity for a rapid reaction and excellent stability towards I^-/I^-_3 electrolyte but limits their application in flexible DSSCs and hence there is a need to explore Pt-free materials for the CE in DSSCs. On the other hand, in order to reduce the cost of DSSCs, conductive polymers and carbon materials, such as PANIs (polyanilines), polypyrrole (PPy), carbon nanotubes (CNTs), graphene, have been widely attempted. However, cheap CE with high catalytic performance and facile fabrication procedures are required for the commercial application of DSSCs. So far different nanostructured carbonaceous materials such as carbon black, CNTs, graphene, polymers and transition metal carbides were synthesized and used as an alternative to Pt CE for DSSCs. Among various nanostructured CE, cost effective electrospun NF and its composites proved to be an exciting alternative materials as CEs in DSSCs and enhance the overall photovoltaic performance of DSSCs.

Joshi et al. synthesized a low-cost electrospun carbon NF (ECNs) CE alternative to Pt in DSSCs[90]. ECNs have been explored as an electrocatalyst and low-cost alternative to Pt for triiodide reduction in DSSCs. The ECN-based cells achieved an energy conversion efficiency (η) of 5.5 % under the AM 1.5 illumination at 100 mW cm^{-2}. The lower cell performance using the ECN electrode were due to lower fill factor (FF) than that of Pt-based cells, probably caused by high total series resistance (R_{Stot}) at ~15.5 Ω cm^2, which was larger than that of ~4.8 Ω cm^2 in the Pt-based devices. *Li et al*. developed high catalytic active one-dimensional CuS/carbon NF (CuS/EC) were fabricated by combining electrospinning technique followed up by hydrothermal process[91]. CuS/EC hetero-architectures demonstrated good performance as CE for quantum dot-sensitized solar cells. *Poudel et al*. reported composite CE made of ECNs and Pt NP[92]. The new ECN–Pt composite had demonstrated as a more efficient electro-catalyst with lower charge transfer resistance (R_{ct}), larger surface area, and faster reaction rate for the reduction of I^-_3 ions than those of conventional Pt in DSSCs. DSSCs using ECN–Pt CE achieved a η of ~8%, which was higher than that of the conventional Pt cells. *Peng et al*. demonstrated a simple electrospinning method to directly deposit conductive 10-amphorsulfonic acid (CSA)-doped polyaniline (PANI) blended with poly(lactic acid) (PLA)composite films (PANI.CSA–PLA) on rigid FTO and FTO-coated poly(ethylene naphthalate) (PEN) substrates as shown in Fig. 8(a)[93]. The rigid and flexible DSSCs demonstrated high photovoltaic efficiency, close to that of sputtered Pt-based DSSCs. Surface morphology showed that the PANI CSA–PLA film was assembled from about 200 nm-diameter NFs, with a uniform thickness of about 2 μm. The photoelectric conversion efficiency of the DSSCs firstly based on such rigid and flexible PANI-CSA–PLA counter electrodes achieved 5.3% and 3.1%, respectively, which was close to sputtered Pt-based DSSCs. In addition, the rigid PANI-CSA–PLA-based DSSC demonstrated good stability and its photocurrent density–voltage (J–V) curves are shown in Fig. 8.

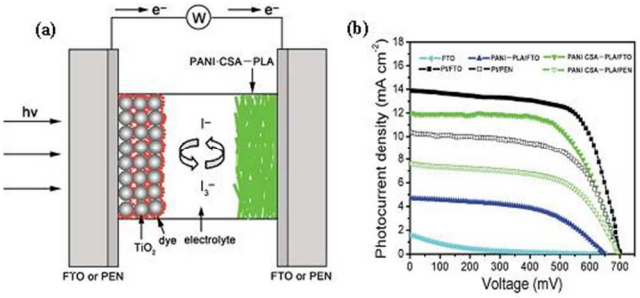

Fig. 8 (a) Schematic diagram of DSSC based on PANI.CSA-PLA NF film on FTO or PEN substrates as the CE. (b) Photocurrent density–voltage (J–V) curves of DSSCs based on FTO glass, PANI–PLA/FTO, PANI-CSA–PLA/FTO, Pt/FTO, PANI-CSA–PLA/PEN, and Pt/PEN counter electrodes respectively, under 1 sun illumination of 100 mW cm^{-2} (AM 1.5)[93].

Park et al. prepared mesoporous multi-walled CNT (MWCNT)-embedded CNFs (MWCNT/meso-ACNF) through various steps of electrospinning, stabilization, carbonization, SiO_2 template etching, and activation[94]. Its mesoporous structure represented surface area of 562 m^2g^{-1} with average mesopore diameter of 27.32 nm and its electrical conductivity increased to 0.19 S/cm. The overall conversion efficiency of MWCNT/meso-ACNF increased to 6.35% with a slightly higher than Pt counter electrode because of its characteristics in promoting the electron and ion transfer, decreasing the resistance of charge transfer and increasing the contact area between liquid electrolyte and CNT/meso-ACNF. *Mali et al*. successfully adopted highly crystalline kesterite Cu_2ZnSnS_4 (CZTS) NF as counter electrodes for dye-DSSCs[95]. The synthesized CZTS NFs using PVP and observed single crystalline crystal structure whereas cellulose acetate (CA) exhibited polycrystalline behaviour. The prepared PVP-CZTS and CA-CZTS counter electrode based DSSC showed efficiency of 3.10% and 3.90%, respectively.

Kim et al. also reported multifunctional crystalline platinum NF (PtNF) web with diameter 40-70nm for FTO free DSSCs[96]. These electrospun PtNF were highly catalytic/transparent and conductive for free electron transport properties acting as counter electrode in DSSC with increased power efficiency of 6.0% and reached up to 83% of that in a conventional DSSC using a Pt-coated FTO glass as a counter electrode. *Park et al.* reported hollow activated carbon NFs (H-ACNF) as catalysts of CE for DSSCs[97]. H-ACNF exhibited high surface area of 1037.5 m^2 g^{-1} with average mesoporous diameter of 17.4 nm. The overall conversion efficiency of H-ACNF was comparable to Pt CE due to its easy promotion of electron and ion transfer, decreasing the resistance of charge transfer, and increasing the contact area between liquid electrolyte and H-ACNF.

Another challenge in conversion DSSC efficiency is poor harvesting of solar light with wavelengths longer than 600 nm,

due to the transmission of incident light through the photoanode. However, inclusion of large particles of size comparable to the wavelength of incident light encourages better light scattering in DSSCs especially from the red part of the solar spectrum. Though this is technologically challenging, light scattering layer approach is an effective and practical method to enhance efficiency in larger DSSC. Electrospun 1D NF provides direct pathway for electron diffusion which can enhance the light scattering properties and possibly enhance the conversion efficiency of DSSCs. Thus, additional scattering layers of large TiO_2 particles, nanorods, and/or NFs have been adopted into photoanodes to improve the light absorbance. Recently, TiO_2 nanostructures with large diameters and high surface areas such as mesoporous microspheres and hemispheres have been used as scattering layers for both increasing the light harvesting efficiency as well as the dye-loading. *Zhu et al.* fabricated nest-shaped TiO_2 (NS-TiO_2) structures by electrospinning and used as an effective scattering layer on the top of TiO_2 nanoparticle electrodes in DSSCs[98]. The NS-TiO_2 scattering layer enhanced the photocurrent of DSSCs due to the enhanced light harvesting which in turn improved the light scattering and lowered electron transfer resistance under one sun illumination (AM 1.5G, 100 mW cm^{-2}), a high efficiency of 8.02% was achieved for the cell with a NS-TiO_2 scattering layer, which had an increased efficiency of 7.1% compared to the cell without a scattering layer (7.49%).

Similarly, *Wang et al.* fabricated double layered SnO_2 NFs / NPs DSSCs using an efficient light scattering layer and blocking layer[99]. Photovoltaic performance of DSSC with single layer SnO_2 NPs (18.5 μm) and double layer SnO_2 NPs (14.5 μm)/NFs (4.0 μm) demonstrated conversional efficiency (η) of 4.30% and 5.44%, respectively. Furthermore, additional SnO_2 blocking layer in double layered photoanode DSSC showed an increase in power conversion efficiency of 6.31% (with J_{sc} of 16.78 mA cm^{-2}, V_{oc} of 711mV and FF of 0.53) which would be mainly due to the faster electron transport rate and lower electron recombination rate between the FTO and the electrolyte. *Chen et al.* synthesized ultraporous anatase TiO_2 nanorods as photoanode with a composite structure of meso and macropores fabricated via a simple micro emulsion electrospinning approach[100]. The porous TiO_2 nanorod based DSSC showed a power conversion efficiency of 6.07% and further porous TiO_2 nanorods with bilayer structured which acted as the light scattering layer exhibited improved efficiency of 8.53%. *Lee et al.* reported electrospun TiO_2 NFs were used as scattering layers on the double-layered TiO_2 NP/TiO_2 NF structure in DSSCs[101]. The double-layered with TiO_2 NF scattering layer played a major role in dye adsorption and light transmission, which improved the absorption of visible light due to the light scattering effects. The 12 mm-thick photoanode composed of a 2 mm-thick TiO_2 NF layer and 10 mm thick TiO_2 NP layer observed 33% higher conversion efficiency than that of DSSCs with only TiO_2 NPs photoanode. *Wu et al.* demonstrated an enhancement in light-harvesting efficiency of the photoanode DSSCs by forming NFs and nanofilm on top of the ZnO nanowire (NW) anode[102]. A 74% enrichment of the efficiency of ZnO NW DSSCs were achieved by reflecting unabsorbed photons back into the NW anode using the novel light-scattering layer of nanofilm. *Zhu et al.* adopted a concept of thin film of rice grain and NFs shaped TiO_2 nanostructures for effective scattering layer on the NP electrodes in DSSCs by electrospinning[103]. Fig. 9(a-b) shows the cross-sectional SEM images of the NP electrodes with the rice grain and NF shaped TiO_2 as the scattering layers with average thickness of the TiO_2NP electrodes was ~10 μm and that of the scattering layers was ~2 μm. With the NF as scattering layer, the efficiency was increased from 6.44% to 7.06%, with the current density increased from 13.6mA cm^{-2} to 14.9mA cm^{-2}. In the case of rice grain structure, the efficiency was increased from 6.44% to 7.45%, with the J_{sc} enhanced from 13.6 mA cm^{-2} to 15.7 mA cm^{-2}. The rice grain-like nanostructures were found to be better in scattering the light with a 15.7% enhancement in efficiency when compared to 9.63% for NFs.

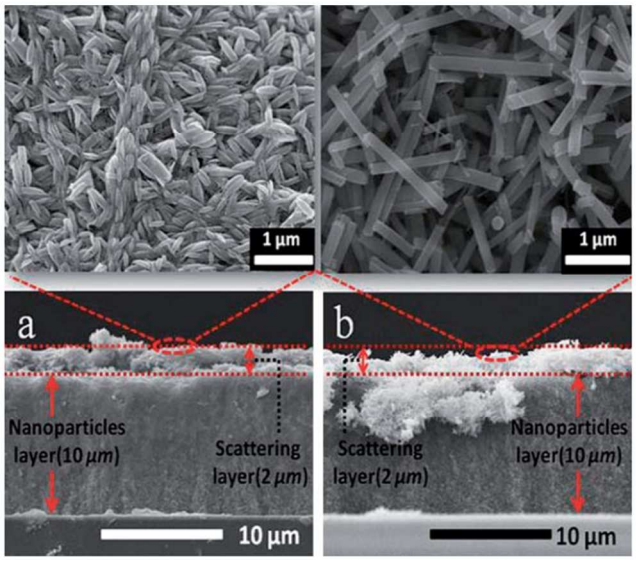

Fig. 9 Cross-sectional SEM images of (a) TiO_2NP–rice grain nanostructure electrode, and (b) TiO_2NP–NF electrode and enlarged images of the scattering layers are shown in top[103].

Joshi et al. reported that the composite made of electrospun TiO_2NFs and TiO_2NPs photoanode had noticeably improved the harvesting of light without substantially sacrificing the dye uptake in DSSCs[104]. The increase in light harvesting had found to be very effective due to Mie scattering resulting from the incorporation of TiO_2NF. The DSSC made using the composite with 15 wt% fibers achieved a J_{sc} of 16.8mA cm^{-2} and η of 8.8% when compared to TiO_2NP alone, which had J_{sc} and η of 11.4 mA cm^{-2} and 6.1%, respectively, for the same photoanode thickness (~7.5 mm).*Chen et al*. reported electrospun NFs constructed of mesoporous nanocrystalline titania with fiber diameters ranging from 194 to 441 nm as light-scattering photoactive materials[105]. The photocurrent−voltage response of NF sample with a scattering band that overlapped with the absorption band of titania exhibited a significant photocurrent increase as a function of the fiber deposition density. *Yang et al*. reported electrospun TiO_2 microspheres (M-TiO_2) as a scattering layer on top of a nanocrystalline TiO_2 (P25) film for CdS QDSC[106]. The power conversion efficiency of 1.49% was achieved for the cell with an M-TiO_2 scattering layer, with an increase of 28.4% compared to the cell without a scattering layer (1.16%).

Further to enhance DSSC efficiency, a very thin metal layer has been applied to form a passive layer and preventing injected dye electron recombination between photoanode and electrolyte. *Naphade et al.* observed enhancement in the performance of dye sensitized solar cells by using in-situ 4–5 nm Au NP (Au NP) loaded TiO_2NF (Au:TiO_2 NFs) as light harvesting layer[107]. A significant enhancement in the efficiency by 25% was achieved with the Au NF light harvesting layer as compared to 12% with the NF layer without any light harvesting layer. *Horle et al.* reported of Nb-doped TiO_2 (TNO) electrospun NFs as a conductive agent in the mesoporous TiO_2layer[108].The TNO NF exhibited an efficiency η increase from 4.8 to 5.8% by the coating. These increases were mainly attributed to J_{sc} by ~15% from 9.7 to 11.2 mA cm^{-2}. Similarly, *Horie et al.* reported electrospun NFs of TiO_2 and Nb-doped TiO_2 (NTO) added to TiO_2 mesoporous layer in the photoelectrode of DSSCs[109]. The short-circuit current density J_{sc} of electrospun NFs of TiO_2 and NTO, was around 6% and 8%, respectively.

In the perspective of searching for pioneer energy conversion systems, third generation photovoltaic quantum dot-sensitized solar cells (QDSSCs) technologies are attracted growing interest as a potential candidate. Specifically, photoanode geometry plays a vital role in shaping the conversion efficiency of the cells through controlling the amount of QD-loading and electrolyte penetration, but also surface recombination and light scattering. Tuning the absorption spectrum of semiconductor quantum dots (QDs), probing the particle size is an efficient way to harvest the entire range of the solar spectrum. In addition, owing to the unique electronic band structure, QDs can overcome the Shockley–Queisser limit of energy conversion efficiency[110, 111].Recently, extending the light harvesting wavelength through panchromatic metal sulphide sensitizers exhibited obvious advantages of cost reduction and efficiency enhancement, owing to their adjustable band gap, high extinction coefficient, large intrinsic dipole moments, and potential processes of multiple exciton generation configurations, and thereby offering new avenues to attain high conversion efficiency. *Jin et al.* reported the fabrication of three dimensional networks of ITO NFs on a conductive glass substrate by electrospinning[112]. Photoactive CdS nanocrystals were directly electrodeposited onto the 3D ITO NF networks which obtained ITO/CdS coaxial NFs as the photoanode of solar cells. The solar cell had attained a conversion efficiency of 1.66% with the highest photocurrent density of 9.27 mA cm^{-2} for pure CdS sensitized solar cells. *Shengyuan et al.* demonstrated a CdS QDSSC featuring CoS counter electrode prepared by SILAR method with an overall power conversion efficiency of nearly 1% in the presence of a methanol-free polysulfide electrolyte[113]. *Sudhagar et al.* reported quantum dot (QDs) decorated highly porous networks TiO_2 nanofibrous electrodes which yielded multiple carrier generations due to the quantum confinement effect[114]. CdS (~18 nm) and CdSe (~8 nm) QDs were sensitized onto electrospun TiO_2nanofibrous electrodes with diameter ~80–100 nm. The photovoltaic performances of single (CdS and CdSe) and coupled (CdS/CdSe) QDs-sensitized with TiO_2 fibrous electrodes were demonstrated in sandwich-type solar cells using polysulfide electrolyte which result in enhanced open-circuit voltage (0.64 V) with 2.69% efficiency. Similarly, *Sudhagar et al.* reported surface treatment approaches to improve the electronic interfaces of quantum dot-sensitized with highly dense, continuous TiO_2 fibrous electrodes[115]. F-ion post-treatment on the TiO_2 fibrous membrane showed the V_{oc} of 0.61 V and J_{sc} of 11.4 mA cm^{-2} with an overall efficiency of 2.8%. Simultaneously, further V_{oc} enhancement also observed after ZnS coating on a sensitizer layer which improved the V_{oc} (0.69 V) by passivating the QDs. Tetrahydrofuran (THF) -ion treatment with the ZnS passivation layer on the QD-sensitizer and TiO_2 fibrous photoanode yielded a high device performance of 3.2% with a remarkable V_{oc} of 0.69 V. *Han et al.* reported facile synthesis of TiO_2 nanotube branched of length ~0.5 μm with thin hollow-NFs as photoanodes in QDSSCs[116]. The hierarchical three dimensional photoanodes exhibited a 3-fold higher η~2.8%, J_{sc} = 8.8 mA cm^{-2} than that of the directly grown nanotube arrays on a transparent conducting oxide (TCO) substrate with η~0.9%, J_{sc} = 2.5 mA cm^{-2}.

Besides TiO_2 NF as photoanode, several other electrospun metal oxides NFs such as ZnO, SnO_2, CuO were used as promising and alternatives light sensitizers to the TiO_2nanostructures. Recently, *Zhang et. al.* reported electrospun nanofibrous ZnO photoelectrodes with tuneable thickness and self-relaxation layer[117]. A maximum energy efficiency of 2.58% was observed for device with a film thickness of 5.0 μm, which had the larger surface area and higher dye loading. Further, calcined ZnO film with 0.2*M* $Zn(OAc)_2$ yielded the η of 3.02%. *Yun et al.* fabricated DSSC based on the Al-doped ZnO (AZO) as NF photoelectrodes with energy conversion efficiency(η) of 0.54–0.55% which had been obtained under irradiation of AM1.5 simulated sunlight(100mWcm^{-2})[118]. Similarly, *Kim et al.* reported directly electrospun ZnO/poly(vinyl acetate) composite NF mats and calcined at 450°C[119]. The DSSCs using ZnO NF of 200-500nm and diameter cores with ~30nm mats exhibited a conversion efficiency of 1.34% under 100mWcm^{-2} illumination. *Kumar et al.* synthesized flower shaped SnO_2 nanostructures by electrospinning for the first time by precisely controlling the precursor concentration in a polymeric solution[120]. The SEM images showed the flower structure made up of fibrils of diameter 80–100 nm, which in turn were made up of particles of size ~20–30 nm (Fig. 10(a-b)).The cell of 15 μm thickness, flower-based DSSC showed a record of V_{oc}~ 700 mV, J_{sc}~7.30 mA cm^{-2}, FF ~59.6% and η of~3.0%, whereas the fiber based DSSC showed V_{oc} ~ 600 mV, J_{sc} of ~3.0 mA cm^{-2}, FF ~8.3 and η= 0.71%, i.e. the flower based device showed ~140% increased J_{sc}, ~16% increased V_{oc} and ~55% increased FF than the fiber based device as shown in Fig. 10(c).The highest IPCE for the devices based on the fibers and flowers were ~12% and 42%, respectively in which 30% increased IPCE observed in later case could be attributed to the enhanced electron density and charge transport efficiency as well as a slightly higher amount of the dye-loaded onto the flower based device.

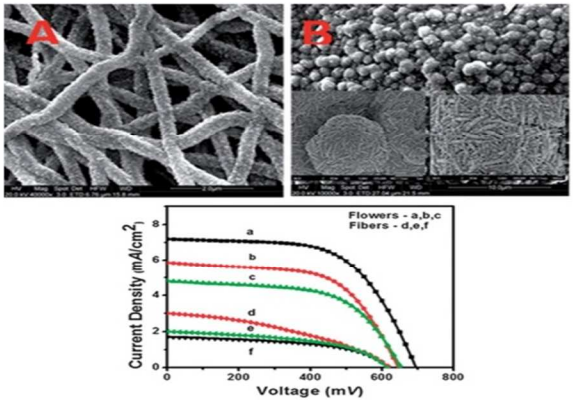

Fig. 10 (a-b) SEM images of SnO_2 fibers and flowers, Insets images in (b) shows the magnified SEM images of the flower morphology, and (c) current–voltage characteristics of the solar cells made using fibers and flowers[120].

Krishnamoorthy et al. reported large-scale production of aligned SnO_2NFs by using multi-nozzle electrospinning[121]. DSSCs using SnO_2NF as the working electrode yielded a J_{sc} of 9.9 mA cm^{-2}, V_{oc} of 0.525 V and η of 2.53% which was comparably 42% higher than that nanowires produced by other methods. *Wang et al.* also fabricated double layered DSSCs using hierarchical 1D SnO_2NFs/NPs which were employed as an efficient light scattering layer[99]. The photovoltaic performance of the double layer SnO_2 NPs (14.5 μm)/NFs (4.0 μm) as light scattering layer in DSSC exhibited 26.3% enhancement compared to a single layer SnO_2 NPs photoanode. *Gao et al.* synthesized branched hierarchical nanostructure of TiO_2 nanoneedles on SnO_2NF network (B-SnO2 NF) which served as model architecture for highly efficient DSSCs[122]. SnO_2NF with diameter ~52 nm showed a power conversion efficiency of 7.06% which had an increase of 26% and 40% compared to B-SnO_2 NF with diameter ~113 nm with efficiency (η) 5.57% and TiO_2 NP (P25) with η of 5.04%, respectively and more than five times as large as SnO_2 NF (1.34%). *Sahay et al.* synthesized electrospun copper based composite NFs using the copper acetate/PVA solution as starting material[42]. The observed the formation of poly-crystalline CuO structure with predominate (111) phase orientation with diameter of ~141 nm. Preliminary results on CuO NFs DSSC with ZnO as the blocking layer exhibited 25% increase in the current density.

Organic solar cells (OSCs) have also been attracted considerable interest as a potential renewable energy device due to its low cost, with lower environmental load and flexibility, and are lightweight compared to the conventional silicon solar cells. Recent advances in developing new organic active layer materials and device processing techniques have led to improvement in conversion efficiencies. *Elumalai et al*. reported usage of electrospun ZnO architecture as electron transporting layer (ETL) which exhibited a high photoelectric conversion efficiency and stability[123]. They developed Inverted bulk hetero junction organic solar cells device structure ITO/ZnO/poly(3-hexylthiophene) (P3HT):[6,6]-phenyl C61 butyric acid methyl ester (PCBM)/MoO_3/Ag. The devices those employed a higher loading of ZnO nanowires showed 20% higher photoelectric conversion efficiency (PCE), which mainly resulted from an enhancement in its fill factor (FF). *Bedford et al.* demonstrated NFs based bulk heterojunction organic photovoltaic (BHJ–OPV) with electron donor–electron acceptor pair poly(3-hexylthiophene):phenyl-C61-butyric acid methyl ester (P3HT:PCBM)[124]. These fibers were then incorporated into the active layer of a BHJ–OPV device, which resulted in improved short-circuit current densities, fill factors, and power-conversion efficiencies (PCE). The best-performing fiber-based devices exhibited a PCE of 4.0%, while the best thin-film devices had a PCE of 3.2%. *Chen et al.* reported patterned electrospun Ag/PVP composite NFs for P3HT:PCBM photovoltaic devices[125]. The composite electrospun NFs were prepared using in-situ reduction of Ag NPs in Ag/PVP via a two-fluid coaxial electrospinning technique which observed 18.7% enhancement in power conversion efficiency of photovoltaic device. *Wu et al.* reported hybrid solar cell based on electrospun ZnO NFs/poly(3-hexylthiophene) (ZnO/P3HT). Improved device efficiency from 0.3% to 0.65% was observed after the CdS modification, which mainly due to the cascaded band structure of the heterojunction that can facilitate charge transfer at the interface and induce higher light absorption in visible region[126]. Similarly, *Wu et al* .also reported organic–inorganic hybrid solar cells based on P3HT and electrospunTiO_2 NFs[126]. The CdS modified layer led to the increase of both open circuit voltage and short circuit current of the device, which were attributed to enhanced exciton dissociation and light absorption. It also suppressed the carrier recombination at the heterojunction which increased the power conversion efficiency of the device for about 50%.Table 1 shows the summary of hierarchical electrospun NFs based DSSCs as photoanodes, counter electrode (CE) and scattering layer (SL). The application of hierarchical NFs such as random aligned, porous, hollow and core-shell with tuneable structures, combined with surface properties showed greater potential of electrospun fibers in enhancing the efficiency of DSSCs, QD-DSSC and OSC over other physical or chemical methods. The results demonstrated that electrospun NFs based on photoanode, CE, electrolyte and SL materials like TiO_2, ZnO, SnO_2, carbon based NF and its composites exhibited stable and high energy conversion efficiency.

Table 1: Summary of hierarchical electrospun NFs based DSSCs as photoanodes (PA), counter electrode (CE) and scattering layer (SL).

Material	Type	Structure	Conditions	Eff. (η%)	Ref
TiO_2	PA	Fiber to rice-shaped to leaf-shaped	NF dia. ~100 nm, Rice dia.~120nm	4.5	75
TiO_2	PA	Porous nanorods	Dia.~ 50 nm	4.56	127
TiO_2	PA	Mesoporous TiO_2NF	Dia. 100–280 nm, Surface areas ~9–100 m^2 g^{-1}	4.96	79
TiO_2	PA	Hollow Mesoporous NF	NF dia. ~ 130 nm, Surface area ~118 m^2 g^{-1}	5.6	128
TiO_2/ ZnO	PA	Core–sheath NFs	Dia.~ 150 nm	5.17	129
TiO_2	PA	Ultraporous rod	-	6.07	100
TiO_2	PA	Nanorods	-	6.2	72
TiO_2	PA	Hierarchicall y structured	-	7.93 %	130

		NF			
TiO_2	PA	Nanorods	Thickness of 14 µm	9.52	[131]
TiO_2-graphene composite	PA		NF dia. ~150 nm	7.6	[132]
ITO/CdS	PA	Coaxial NF	-	1.66	[112]
TiO_2	PA	Porous networks NF	NF dia. ~80–100 nm	2.69	[114]
Al-doped ZnO	PA	NF	-	0.55	[133]
ZnO	PA	NF	Dia. ~200-500nm	1.34	[119]
ZnO	PA	NF	Thickness of 5.0 µm	3.02	[117]
SnO2	PA	Flower shaped nanostructure	Dia.~80–100 nm, Particles size ~20–30 nm	3.0	[134]
SnO_2	PA	Aligned NF	-	2.53	[121]
SnO_2	PA	NF network	Dia.~52 nm	7.06	[122]
Anatase TiO_2	SL	prickle-like NF	Surface area ~ 154 $m^2 g^{-1}$	7.86	[135]
TiO_2	SL	Nest-shaped	-	8.02	[98]
TiO_2	SL	NPs/ NFs	NF layer ~2 mm NP ~10 mm	33% higher than TiO_2 NPs	[101]
SnO_2	SL	NFs/ NPs	Double layer NPs (14.5µm) /NFs (4.0 µm)	5.44	[99]
TiO_2	SL	Rice grain- and NF	Rice-grain and NF layer thickness ~2 µm	7.45 7.06	[136]
TiO_2	SL	Ultraporous nanorods	Bilayer porous nanorods	8.53	[100]
TiO_2	SL	NF/NPs		8.8	[137]
Pt	CE	NFs	Dia.~ 40–70 nm	6.0	[96]
Cu_2ZnSnS_4	CE	NFs	Strong absorption in 300–550 nm	3.10 and 3.9	[95]
Carbon	CE	NFs	Dia. ~ 250 nm, Surface area ~100 $m^2 g^{-1}$	5.5	[138]
PANI CSA-PLA	CE	NFs	Dia. ~200 nm	5.3 and 3.1	[139]
MWCNT-carbon NF	CE	Mesoporous NF	Dia. ~27.32 nm, Surface area ~ 562 $m^2 g^{-1}$	6.35	[140]

4. Photocatalysis

In recent years, there has been an increasing demand of clean water globally due to growing urbanization, industrial and man-made pollutions. To overcome these issues, researchers have developed various advanced treatment processes to treat the wastewater effectively and re-utilizing them for human immediate consumption and industrial needs. Among the treatment process, semiconducting metal-oxide based photocatalytic treatments have received a greater attention due to its low-cost, recyclability, reusability and environmental friendly. The metal oxides with novel properties can be easily synthesized from electrospinning due to simple processing and cost-effective process. These metal oxides have been widely utilized to remove the organic contaminants and microorganism present in the wastewater.

In photocatalysis, semiconducting metal oxides (MOs) such as TiO_2, ZnO, Fe_2O_3, CeO_2 and WO_3NFs have been used as sensitizers/catalysts for light induced redox process to photodegrade the toxic and hazardous compounds[141, 142]. Generally, upon photo-irradiation of semiconducting MOs with photons of energy $h\nu \geq E_g$, an electron, e_{CB}^- is promoted from the valence band (VB) into the conduction band (CB), leaving a hole behind, h_{VB}^+ . These generated electron-hole pairs are powerful oxidizing and reducing agents (eqn. 1 & 5), and creates reactive radicals (OH_{ads}^{*-}, O_2^{*-}) in the photocatalytic reactions (eqn. 2, 3 & 4). These highly reactive radicals then react with pollutants and degrade them into non-toxic compounds[143-145].

$$MO + h\nu \longrightarrow e_{CB}^- + h_{VB}^+ \quad \cdots (1)$$
$$H_2O \leftrightarrow OH^- + H^+ \quad \cdots (2)$$
$$h_{VB}^+ + OH_{aq}^- \longrightarrow OH_{ads}^{*-} \quad \cdots (3)$$
$$e_{CB}^- + O_2 \longrightarrow O_2^{*-} \quad \cdots (4)$$
$$h_{VB}^+ + pollutants \longrightarrow pollutants^* \quad \cdots (5)$$
$$pollutants^* + (O_2^{*-}, OH^{*-}) \longrightarrow degraded\ products \quad \cdots (6)$$

There are several factors affecting the efficiency of the photocatalysis. The life time of reactive radicals/species is generally found to be in tens of nanoseconds, and thereby the excited electron and holes should be effectively utilized, otherwise electron-hole recombination occurs and diminishes the efficiency of photocatalysis. In addition, the surface area and porous nature of photocatalysis also play a vital role to improve the interaction between pollutants and MOs for effective degradation. Considering these factors, researchers are focused to address these issues by synthesizing one dimensional semiconducting MO materials with novel properties like porous morphologies, higher surface areas, and higher crystallinity[141, 146-148].

Anatase based TiO_2 with band gap of 3.2eV have been widely used as an effective photo catalyst for wastewater treatment. *Zhang et al.* employed coaxial electrospinning to synthesize hollow mesoporous 1D TiO_2NFs with a high surface area of 118 m^2g^{-1}[82]. The hollow mesoporous TiO_2NFs with closed packing of grains demonstrated faster electron diffusion and longer electron recombination time than regular TiO_2NFs and P25 NPs. The hollow mesoporous TiO_2NFs with higher surface area had better interaction and diffusion of rhodamine B (Rh B) dye and resulted in an increased catalytic activity over P25 TiO_2 nanocatalysts. *Ganesh et al.* developed self-cleaning TiO_2 coatings comprised of rice-grain shaped nanostructures on glass substrates. The coatings were transparent and exhibited a higher photocatalytic activity than spray-coated P25 NPs for photodegradation of alizarin red dye, which was due to the single crystalline nature and high surface area[149]. *Liu et al.* investigated the role of morphology of ZnO NF in the photodegradation of Rh B and acid fuchsine under visible light[150]. The porous structure of ZnO NFs improved the interaction between the dye molecules and the catalyst surface

areas that were contacting while the aggregation of ZnO NP in the solution lowered the photocatalytic efficiency. *Sundaramurthy et al.* fabricated novel nanobraid and nanoporous morphologies of pure ceramic α-Fe_2O_3 nanostructures by varying precursor concentrations[151]. The novel morphologies of α-Fe_2O_3 exhibited superior photocatalytic performance of up to 91.8% and 90.8% against congo red in shorter photo-irradiation period of 140 min (Fig. 11).

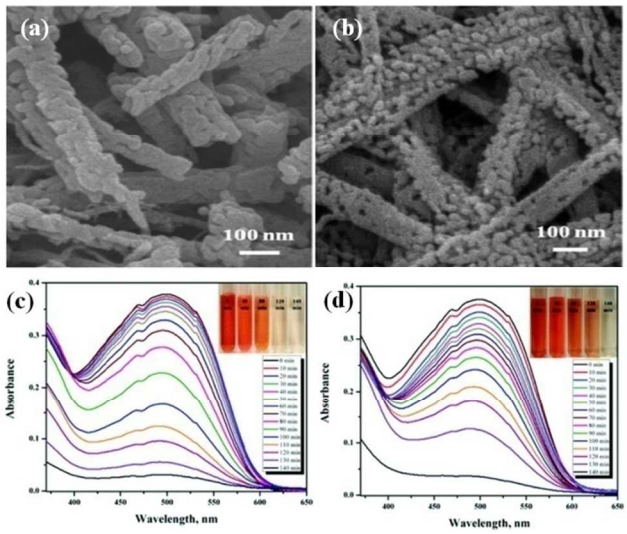

Fig.11 FESEM images of (a) nanobraid and (b) nanoporous α-Fe_2O_3 nanostructures after calcining the as-electrospun 4 wt% & 6 wt% iron acetylacetonate/PVP composite NFs. UV-visible absorbance spectra of photodegradation of congo red in the presence of (c) nanobraids, and (d) nanoporous α-Fe_2O_3 nanostructures[151].

The presence of porous surface and smaller crystallite size of α-Fe_2O_3 nanostructures acted as active catalytic centre and played the vital role for allowing the effective interaction between congo red and α-Fe_2O_3, and thereby enhancing the photosensitized catalytic photodegradation. *Zhao et al.* synthesized Bi_2WO_6NFs, a strong acid oxide and showed its ability to photodegrade the methylene blue around 94.8% under visible light exposure of 3.5 h comparing with the Bi_2WO_6 powder which exhibited photodegradation around 44.1%[152]. The band gap narrowing and the absorption edges of 1D Bi_2WO_6 NFs shifted towards the infrared region which in turn broadened the absorption ability in the visible light region. In addition, the surface active sites in the fibers were significantly increased than the counterpart, which in turn improve the absorption of hydroxide free radicals of methylene blue and reduced the distance between catalyst and dye, thereby utilizing photogenerated holes, electrons and radicals effectively. Electrospun BiOI nano plate like structures was fabricated and tested their ability to degrade Alizarin Red S (ARS) dye under UV light irradiation[153]. The photocatalytic activity was also dependent on morphology [154] and structures[155]. However, the usage of MOs like TiO_2 (3.2 eV for anatase) and ZnO (3.37 eV) possessing large band gap was limited by the photoresponse in UV region only, but only a small UV fraction (<4%) of the total solar spectrum reaches the earth surface[145, 156]. In order to extend the photoresponse of MOs to visible region, many research groups focused on doping with transition metal ions or non-metal elements, such as V, Co, Ag, Au, Fe, C, N, S, or I[157-160]. *Zhang et al.* successfully doped V ions into TiO_2NFs by electrospinning together the vandium and TiO_2 precursors and calcining at 500 ^oC[161]. The fibers retained anatase phase after calcination and XRD results confirmed the successful incorporation of V^{4+} or V^{5+} ions into the crystal lattice of anatase TiO_2NFs and also showed the slight variations in crystallite size with increase in doping (Fig. 12(a-b)). The V doping led to extend the visible light absorption of TiO_2NFs (Fig.12(c)) and 1.0 and 5.0 wt% V-doped TiO_2 NFs possessed higher activity for the photodegradation of methylene blue (MB) and these NFs also recycled without a decrease in the photocatalytic activity. *Xu et al.* demonstrated the doping of TiO_2 NFs with metals like Bi shifted the absorption spectra of TiO_2 into visible light region and effectively utilized the lower energy photons for photocatalytic reactions[162]. The Bi-doped TiO_2 NFs exhibited enhanced 88.8 % photodegradation of Rh B by photosensitization effect and better photocatalytic activity of 56.1% phenol degradation compared with TiO_2 NFs and P25 TiO_2 NPs. *Lin et al.* fabricated a unique dimer-type heterostructure of Ag-ZnO NFs using electrospinning and the coupled heterojunction structure promoted the charge separation and photon efficiency, allowing both the photogenerated electrons and holes to participate in the overall photocatalytic reaction[163]. The photocatalytic activity for photodegradation of RhB was enhanced by a factor more than 25 for Ag-ZnO NFs comparing with pure ZnO NFs. *Kim et al.* synthesized graphene/carbon composite NFs (CCNFs) with TiO_2 NPs uniformly coated on electrospun CCNFs[164]. These composites NFs were very active photocatalysts in the photodegradation of MB under visible light irradiation and the NFs could be recycled back for multiple degradation cycles without a decrease in the photocatalytic activity. The graphene acted as an electron acceptor and a photosensitizer, causing an increase in the photodegradation rate and reducing electron–hole pair recombination.

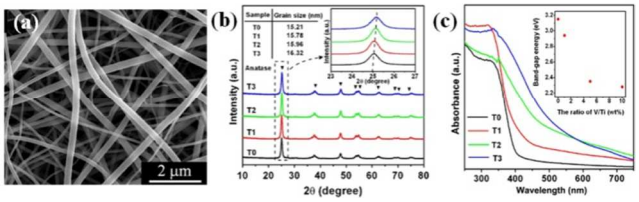

Fig 12 (a) SEM image of V-doped TiO_2NF, (b) XRD patterns of TiO_2 and V-doped TiO_2NFs: TiO_2NFs (T0); 1.0 wt.% V-doped TiO_2NFs (T1); 5.0 wt.% V-doped TiO_2NFs (T2); 10.0 wt.% V-doped TiO_2NFs (T3) and UV–Vis diffuse reflectance (DR) spectra of TiO_2 and V-doped TiO_2NFs[161].

1D TiO_2 regular NFs were prepared by electrospinning and surface nitridation treatment in NH_3 environment[165]. These 1D nanostructures proved their extended visible-light absorption and showed the performance of photocatalytic activity for N–TiO_2 NFs exceeding above by a factor of 12 from that of pure TiO_2 NFs for degradation of methylene blue dye. *Zhang et al.* demonstrated the improved performance of core/shell NFs of TiO_2@carbon embedded with Ag NPs (TiO_2@C/Ag) to photodegrade the Rh B and methyl orange (MO) compared with the pure TiO_2 NFs, TiO_2@carbon core/shell NFs and TiO_2/Ag NFs under visible light irradiation[166]. This significant enhancement in the photodegradation was due to the good light absorption capability and high separation efficiency of

photogenerated electron–hole pairs based on their photo-synergistic effect. Though the above approaches partly improve the photocatalytic activity of MOs, some issues like the thermal stability of doped materials, photo-corrosion, lattice distortion, and increase in the carrier recombination probability need to be addressed[167-169]. These issues can be addressed by coupling with other narrow band gap semiconductors to serve as the sensitizer to absorb visible light. *Liu et al.* employed TiO_2/ZnO composite NFs for the photodegradation of RhB and phenol under photoirradiation of UV light[170]. By blending ZnO into TiO_2 lead to the formation of a new crystallite $ZnTiO_3$, which improved the absorption efficiency of ultraviolet light with an increase in absorption edge of 20 nm and also reduced the hole–electron pairs recombination because of the coupling effect between TiO_2 and ZnO grain-like composite NPs. *Shang et al.* developed a hierarchical hetero-nanostructures of three-dimensional multicomponent oxides of Bi_2WO_6/TiO_2 by combining electrospinning and hydrothermal approach[171]. The multicomponent oxide three dimensional hetero-nanostructures exhibited enhanced photodegradation of Rh B dye in visible range than that of bulk Bi_2WO_6/TiO_2 powder, the Bi_2WO_6 NPs, and TiO_2 powder (Fig. 13(a-b)). The enhancement in the photocatalytic activity was due to higher surface area, smaller grain size which reduced the recombination of photogenerated electron-hole pairs and the matching band potentials of hierarchical hetero-nanostructures.

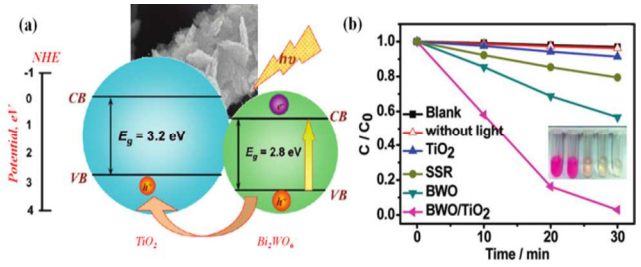

Fig. 13 (a) Schematic diagram for energy band matching and electron-hole separations of Bi_2WO_6/TiO_2 and (b) Photocatalytic degradation of Rh B in the presence of bulk and electrospun Bi_2WO_6/TiO_2 hierarchical hetero-nanostructure under visible-light irradiation[171].

Zhang et al. created 1D electrospun NFs of p-type NiO/n-type ZnO NFs with different molar ratios and studied the photocatalytic activity of Rh B[172]. Upon photoirradiation of UV light (on p-n NiO/ZnO heterojunction (Fig. 14(a-b)) led to the efficient transfer of photogenerated electrons from the conduction band (CB) of p-type NiO to n-type ZnO and photogenerated holes to the valence band (VB) of p-type NiO due to the formation of an inner electric field (Fig. 14(c)). The increasing trend in the photocatalytic reactivity was observed in the order of NiO < ZnO < TiO_2< NiO/ZnO NFs.

The surface photovoltage spectroscopy also confirmed that the efficient charge separation between NiO/ZnO heterojunction, which led to an increase in the lifetime of charge carriers, thereby enhancing efficient interfacial charge transfer across the NiO/ZnO heterojunction and accounted for the higher photocatalytic activity (Fig. 14(d)). *Liu et al.* also fabricated a novel NF structure of photocatalyst consisting of TiO_2 and SnO_2, by side-by-side dual spinneret approach in simple electrospinning process[173]. This bicomponent TiO_2/SnO_2 NF demonstrated an improved photocatalytic activity for the photodegradation of Rh B than the pure TiO_2 NF in a shorter period of time. In TiO_2/SnO_2 heterojunction structure, the band gap matching and exposed morphologies promoted the charge separation of photogenerated electrons and holes, allowing both the photogenerated electrons and holes to participate in the overall photocatalytic reaction and effectively improve the photodegradation.

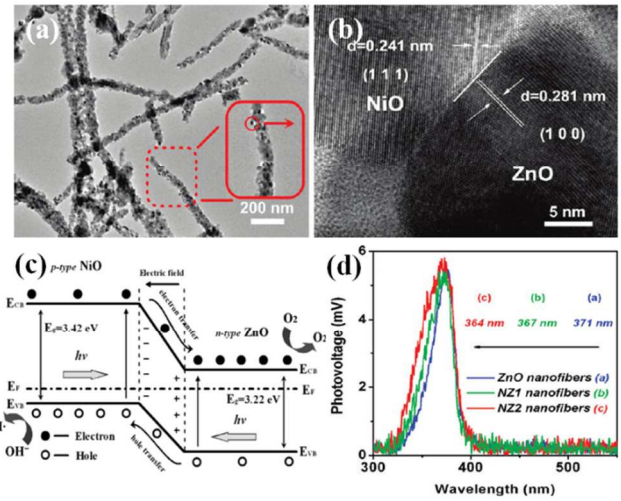

Fig. 14 (a) TEM image of electrospun *p*-type NiO/*n*-type ZnO NFs after calcining at 550 °C for 2 h, (b) HRTEM image of heterojunctions, (c)schematic diagram showing the energy band structure and electron-hole pair separations and (d) surface photovoltage spectroscopy of ZnO and NiO/ZnO heterojunction NFs synthesized at different molar ratios[172].

Table 2: Summary of commonly employed electrospun nanostructures for photocatalysis. *(Abbreviation: Rh B: Rhodamine B; MO: Methyl Orange; MB: Methylene Blue; AO7: Acid Orange II; MWCNT: Multiwall carbon nanotube)*

Review

Cite this: DOI: 10.1039/c0xx00000x

www.rsc.org/xxxxxx

Photocatalysts	Dye (concentration)	Light	% Degradation	Time (min)	Ref.
TiO_2NFs (0.1 wt%)	Rh B (2.5×10^{-5} mol/L)	UV lamp, 8 W	100%	40	174
TiO_2 hollow NFs (0.1 wt%)	Rh B (20 mg/L)	Visible light, 200 W	100%	90	82
TiO_2-Graphene NFs (0.01 wt%)	MO (100 gm/L)	UV (Mercury lamp), 125 W	82%	300	80
S-doped TiO_2NFs (10 wt%)	Rh B (15 mmol/L) Phenol (200 mmol/L)	Visible (Xenon lamp), 500 W	89% 75%	120 120	175
V-doped TiO_2NFs (0.08 wt%)	MB (10 mg/L)	UV (Mercury lamp), 50 W	98.9%	60	161
TiO_2/$CoFe_2O_4$NFs (0.55 wt%)	Phenol (22.2 mg/L)	UV (Mercury lamp), 300 W	36%	210	176
TiO_2/CuO NFs (4 wt%)	AO7 (20 mg/L)	UV (Mercury lamp), 400 W	100%	20	177
In_2O_3−TiO_2NFs (5 wt%)	Rh B (10 mg/L)	Visible (Xenon lamp), 500 W	90%	240	156
$Cd_{1-x}Zn_xS/TiO_2$ heterostructures (10 wt%)	Rh B (10 mg/L)	Visible (Xenon lamp), 500 W	91%	60	178
SnO_2/TiO_2 core/shell NFs (4 mg)	Rh B (5 mg/L)	UV (Mercury lamp), 3 mW/cm^2	89%	150	179
WO_3/TiO_2 Core/Shell NFs	MB (3×10^{-5} M)	UV & Visible (LED lamp) 128 mW/cm^2	70.3%	1333	180
TiO_2/ZnO/Au NFs (1 wt%)	MO (10 mg/L) 4-nitrophenol (10 mg/L)	UV (Mercury lamp), 50 W	96% 96%	30 40	181
ZnO NFs (0.05 wt%)	MB (2 mg/L)	UV (Mercury lamp), 250 W	90%	180	182
Ag-ZnO NFs (0.1 wt%)	Rh B (2.5×10^{-5} mol/L)	UV lamp, 8 W	100%	50	163
ZnO/$BaTiO_3$NFs (0.1 wt%)	MO (10 mg/L)	UV (Mercury lamp), 50 W	100%	90	183
ZnO – Carbon NFs (0.1 wt%)	Rh B (10 mg/L)	UV (Mercury lamp), 50 W	96%	50	184
ZnO-SnO_2NFs (0.25 wt%)	MO (20mg/L)	UV (Mercury lamp), 500 W	100%	20	185
N-doped ZnO - SnO_2NFs (2.5 wt%)	Rh B (4×10^{-5} mol/L)	UV (Mercury lamp), 300 W	100%	150	186
MWCNT-doped ZnONFs (5 wt%)	MB (1×10^{-5} M)	UV lamp, 15 W	24%	120	187
CeO_2–ZnO NFs (5 wt%)	Rh B (5×10^{-5} M)	UV lamp, 15 W	98%	180	188
NiO/ZnO NFs (1 wt%)	Rh B (10 mg/L)	UV (Mercury lamp), 2.85 mW/cm^2	99.7%	50	172
α-Fe_2O_3NFs (5 wt%)	MB (10 mg/L)	UV (Mercury lamp), 300 W	100%	60	189
Fe_2O_3-doped TiO_2 NFs (0.1 wt%)	MB (10 mg/L)	UV (Mercury lamp), 300 W	100%	30	190
$Bi_4Ti_3O_{12}$NFs (1 wt%)	Rh B (6 ppm)	Visible (Xenon lamp), 500 W	89%	240	191
Bi_2WO_6 nanostructures (30 wt%)	MO (20 mg/L)	Visible (Xenon lamp), 500 W	96%	100	192
$LaCoO_3$NFs (0.1 wt%)	Rh B (2 mg/L)	UV (Mercury lamp), 500 W	99%	50	193
SnO_2 hollow microtubes (1 wt%)	Rh B (10 mg/L)	UV (Mercury lamp), 50 W	~100%	90	194

The nanostructured Bi_2WO_6 coupled with TiO_2, the performance for photodegradation of organic compounds was enhanced significantly. The new generation photocatalysts with tungsten and TiO_2 was prepared by the thermal hydrolysis of aqueous solutions of peroxo complexes of titanium and tungsten, which enhanced the reaction rates for photodegradation of Orange II dye in UV and visible regions of the spectrum[195]. Similarly, several researchers attempted to synthesize the combination of different metal oxide nanostructures with band gap matching like TiO_2/CdO[196], CeO_2/ZnO[188], ZnO/SnO_2[197], In_2O_3/TiO_2[156],CeO_2/TiO_2[198], TiO_2/SiO_2[199], ZnO/$BaTiO_3$[183], Bi_2S_3/TiO_2[200] and ZnO/CdO[201] using electrospinning or with combination of electrospinning and other approaches like hydrothermal. By utilizing the synergistic properties from the combination of metal oxides, lead to improve the light absorption, increase the charge separation and reduce the recombination of electron-hole pairs, and thereby enhancing the photodegradation of organic pollutants and dyes effectively under UV and visible light photoirradiation. Table 2 shows the summary of different electrospun metal oxide nanostructures employed in photocatalysis of wide range of dyes and pollutants. Irrespective of the intensity of light and time of exposures, these metal oxides exhibited photocatalytic activity under both UV and visible light depending on the bandgap properties. However, the electrospinning offers an added advantage of improving the visible-light photocatalytic activity of metal oxides, and coupling metal oxides with other conductors or semiconductors by doping or forming core-shell nanostructures to promote the separation of photoexcited electron-hole pairs by the mutual transfer of photogenerated electron or holes in the heterojunction, thus to extend the light-response range. The eletrospun photocatalysts had also shown the excellent recyleability for number of times as photocatalysts without any deterioration in the photocatalytic effect.

5. Hydrogen energy harvesting from nanostructured photocatalyst

5.1 Hydrogen energy production

Nanotechnology is a fast growing scientific advancement for the present and future energy requirements, since the nanostructured semiconductor materials (Si nanowires and TiO_2), facilitates cost reduction in device processing and effective enhancement in energy conversion efficiency. Several research groups focussed on preparation of low cost nanomaterials and to obtain high energy efficiency[58, 202, 203]. The nanostructures have high specific surface area (provides the active sites) compared to the bulk silicon based photovoltaics (PVs)[204, 205]. Obviously the cost of the nanomaterials goes down than the bulk materials and efficiency is also quite promising. The facile synthesis methods for the production of nanostructured materials are demonstrated to their cost reduction compared with the expensive epitaxial growth of thin-film solar cells[206-210]. 1D nanofibers (NFs) has already proven their importance in electronics, optoelectronics, optical sensing, photo dye degradation and energy harvesting technologies[211]. Functional electrospun NFs exhibited numerous optical[212-215] and/or electronic[216-218] properties in nanoscale dimensions. The electrical transport, optical, and photocatalysis properties were closely related to the electronic band gap of the materials[219, 220]. In addition, TiO_2 electrospun NFs showed enhanced crystallinity, high surface area, and photocatalytic activity (PCA) for hydrogen evolution compared by hydrothermal synthesis [221]. The electrospun NFs with high specific surface area facilitated the effective absorption of emitted light, it can be potentially useful in solar energy conversion especially in metal oxides (TiO_2)[214]. In general, by the use of suitable 1D NFs structures can trap photons more effectively with the appropriate geometrical configuration during the generation of excitons (e^-/h^+). The overall dimensions of the nanostructures were similar to the carrier diffusion lengths to facilitate the collection of free carriers in the exciton separation process. The effective exciton generation and charge separation resulted in increasing energy conversion efficiency[209, 222, 223]. Despite the length of 1D nanomaterials ranging from hundreds of nanometres to tens of micrometres, they can scatter light as effective as the large NPs[224, 225]. *Lee et al.* reported the ZnO nanorod arrays can serve as an effective anti-reflection coating in the long range of wavelength from 400 to 1200 nm, due to their regular textures, morphology and nanoscale dimensions[226].

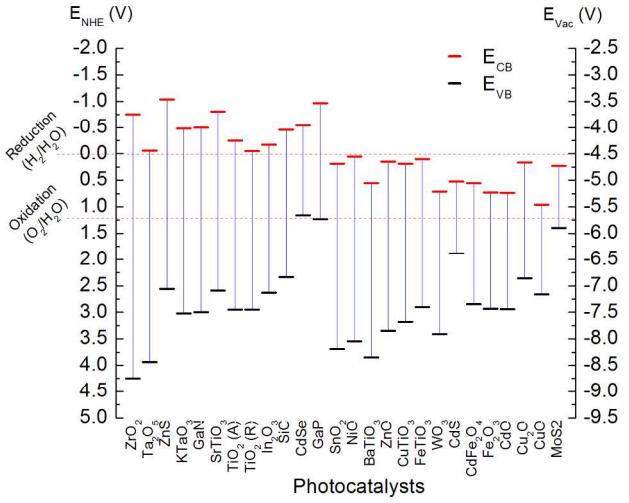

Fig.15 Relationship between absolute CB and VB energy levels for photocatalyst with respect to normal hydrogen electrode (NHE) potential and vacuum energy (V_{ac}).

5.2 Principle mechanism

The first attempt on photo electrochemical hydrogen production by splitting of water was reported in early 1972 by Fujishima and Honda[227]. Single crystalline TiO_2 wafers as working electrode and platinum block as counter electrode, they found that the H_2 and O_2 generation at counter and working electrodes, respectively. They suggested that by adding reducible ion species into counter electrode lead the more currents produced, resulting in high efficiency of water splitting via electrolysis. In recent years, many researchers explored semiconductor photocatalytic hydrogen conversion[228,229]. The photocatalytic hydrogen production requires essential photogeneration of hole/electron pairs. The basic mechanism of photocatalytic water-splitting subjected to several intermediate processes: (a) absorption of photons, (b) recombination, separation, migration, trapping, and transfer of excited charges, and (c) surface chemical reactions.

All these specifications would be affected the final generation of H_2 from the photocatalyst materials. In general, the electrons in the VB of photocatalyst are excited to the CB by irradiation of photon energy, while the holes are left in the VB by creating e^-/h^+ pairs which are referred as photoexcitons. These photoexcited electrons and holes separate and migrate to the surface of the photocatalyst. The list of the some photocatalysts and their valance band (VB) and conduction band (CB) are presented in Fig.15, with respect to standard hydrogen electrode (E_{SHE}) and vacuum (E_{vcc}). As presented in Fig. 15, the photocatalysts with suitable band gap whose electronic structures match well with the redox potential of water to convert into H_2 and O_2 molecules. The band levels of oxide materials generally change with pH for water-splitting. Despite some of the semiconductors which had suitable E_g for visible light response, but not active for the watersplitting were considered as photocorrosives[230]. For example, Cds, and WO_3were fall into photocorrosive category, since their conduction band minima was at very low level and the band structures was just thermodynamic requirement but not a suitable condition of H_2 evolution. Therefore, the suitable band gap engineering was absolutely required for the design of appropriate photocatalysts for H_2 generation.

5.3 Hydrogen generation from photocatalysts

In photocatalytic water-splitting for H_2 production, electrons in CB are most important which reduce protons to hydrogen molecules. However, the CB level must be negative than the hydrogen evolution level to initiate H_2 production[228]. Metal ion-insertion or dye sensitizations were the two methods to extend the activation of TiO_2 to visible light activation. The early experimental works of several researchers focused on the correlation between visible light absorption and photocatalytic activity in nitrogen doped TiO_2 photocatalysts. By recording XPS spectra, the state of N 1s was revealed with two main peaks at 396 and 400 eV. However, different groups reported that the nitrogen doping caused for each peak with N-O, interstitial N, and N-H complexes[231-234]. The nature of the nitrogen related defect associated with visible light absorption remains challenge. *Wu et. al.* reported that the nitrogen doped TiO_2 NFs decorated with approximately 2 nm diameters of Pt NPs tested for hydrogen generation at different wavelengths[235]. The catalysts were found more effective in production of hydrogen energy exhibiting conversion efficiencies of 3.6 % and 12.3 % for 365 nm and 312 nm of UV light irradiation, respectively. Fig. 16(a-b) represents the hydrogen evolution from the nitrogen doped TiO_2NFs under UV-A and UV-B irradiations, respectively. Gaseous N_2 was bubbled at flow rate of 400 mL/min, served as purging gas for production of gaseous state collection.

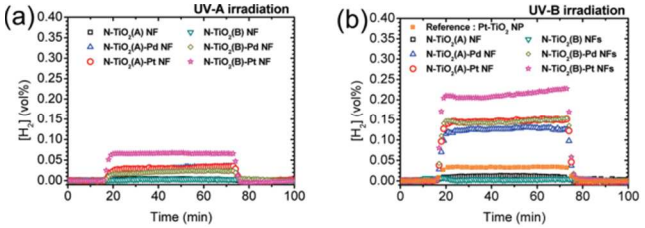

Fig. 16 Hydrogen evolution from ethanol/water mixture (molar ratio 1:3) over parent and noble metal loaded (1.0 wt %) catalyst materials (100 mg each) under (a) UV-A (1.54 W) and (b) UV- B (1.46 w) irradiation[235].

By employing thermodynamic approaches, *Varley et al.* attempted to explain nitrogen impurities on visible light absorption in TiO_2 and found that the nitrogen impurities gave rise to sub-band gap absorption which was clearly attributed to substitutional N, not from interstitial nitrogen[236]. *Sun et al.* synthesized TiO_2 co-doped with Cerium/N and found that the enhancement in the lattice distortion caused the high production rate of hydrogen[237]. Due to the formation of N-Ti and N-Ti-O bonding, the band gap energy was narrowed and resulted in the extended absorption edge towards visible region. These co-doped photocatalysis was stable for increased amount of hydrogen production with longer time periods. Electrospun NF composites for hydrogen generation has demonstrated by using the PVDF and ionic liquids[238]. The catalytic ionic liquids were used only with PVDF for electrospinning. It shows complete release of hydrogen could be achieved by composite NFs.

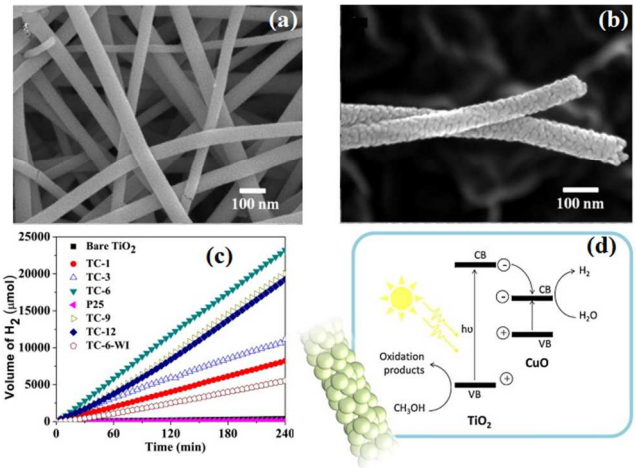

Fig. 17 (a) FESEM images of TiO_2-CuO at 6 mol% of Cu nanofibers (b) high magnification FESEM image of of TiO_2-CuO at 6 mol% of Cu nanofibers (c) Photocatalytic H_2 evolution withing 4h of irratiation time and (d) Schematic illustrationfor the photocatalytic H_2 generation over theTiO_2/CuO heterojunctions[239].

Lee et al reported enhanced photocatalytic hydrogen production from TiO_2/CuO electrospun NFs which has high surface area, visible light absorbance[239]. The hetero junctions between TiO_2 and CuO observed good separation of electrons and holes. The mixed semiconductor (TiO_2/CuO) electrospun NFs at low and higher magnifications are presented in Fig. 17(a-b). The reported photocatalytic H_2 generation under UV light irradiation over 4h of time presented in fig 17(c). At certain level of CuO dopings, the hydrogen production rate has reached maximum and then the generation rate got reduced. The band alignment scheme is presented in fig 17 (d) for the better understanding of the electron and hole transportation. The same authors reported that the TiO_2/CuO composite fibers have multifunctional ability for photocatalytic organic dye degradation and efficient H_2 generation from dye waste water[177]. The composite fibers exhibited excellent synergy effects like (a) large specific surface area (b) absorbance towards higher wave length regions (c) continuous and long nanofibers for efficient charge transfer (d) heterojunctions can enhance the separation of e/h and (e) second metal oxides could serve as co-catalysts for H_2 generation. Fig. 18 (a & b), shows the defect free TiO_2/CuO electrospun composite nanofibers at low and higher

magnifications, these nanostructures were the candidate for a promising photocatalytic applications as well. Fig 18(c) shows the e/h transfer pathways within the composite nanofibers (TiO_2/CuO). Once the photon is absorbed by the catalyst surface, due to the potential difference the electrons were transferred from CB of TiO_2 into the CB of CuO in the heterjunctions. consequently, the excess of electrons which have accumulated in the CB of CuO would cause a negative shift in its Fermi level; rendering higher electron availability for interfacial transfer to H^+ in solution to produce H_2.

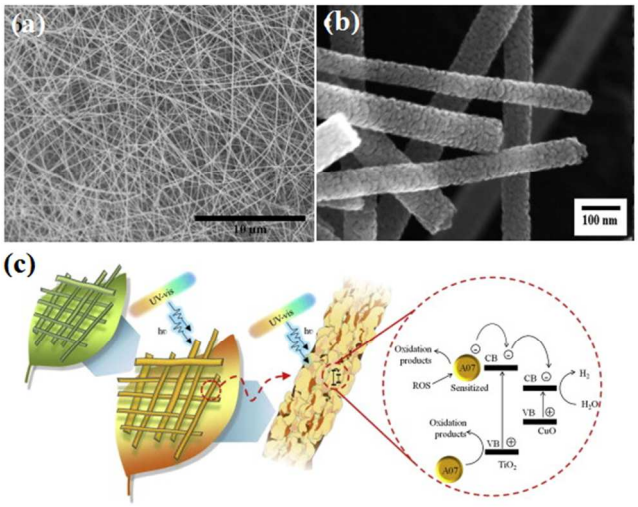

Fig. 18 FESEM images of the TiO_2/CuO nanofibers at (a) low and (b) higher magnifications and (c)Schematic representation of the photo-generated e/h transfer between the TiO2/CuO heterojunctions[177].

Chuangchoteet al. reported a highly efficient photocatalytic hydrogen generation by using TiO_2 electrospun NFs in combination of sol-gel methodology[221]. The hydrogen energy production rate significantly depends on the surface area, crystallinity, higher photocatalytic activity and calcination temperatures. The morphology structures of the electrospun NFs did not affect much upto 400 °C, as they are still in fibrous nature and which is observed from Fig. 19(a-b). However, the fiber diameters are shrunk and alignment of the fibers improved from 400 to 500 °C (Fig. 19(c-e)). Further increase in temperature upto 700 °C, the fiber structures converted into large size interlinked particles (Fig. 19(f-g)). The calcinations temperature and phase transition played a crucial role in determining the amount of hydrogen produced. The electrospun NFs calcined at 450 °C resulted in predominant anatase TiO_2 phase and it led to high amount of hydrogen production (270 µmol/g, under UV light). The electrospun NFs showed highest hydrogen evolution compared to the samples prepared by hydrothermal method[240]. The XRD patterns of the TiO_2 calcined at different temperature are shown in Fig. 20(a), and the corresponding hydrogen evolution with respect to the irradiation times are shown in Fig. 20(b).

A wise combination of photocatalyst (semiconductor) with other semiconductor such as SnO_2[241], could promote UV light absorption. Electrospun Strontium titanate ($SrTiO_3$) NFs can also be utilized for the photocatalytic hydrogen generation via water splitting[242]. The obtained hydrogen was ca.1100 and 300 µmol within 200 min from $SrTiO_3$ and TiO_2 electrospun NFs respectively. *Lee et al.* reported experiments studies on SnO_2 doped TiO_2 electrospun nanfibers and studied their photocatalytic hydrogen conversion from water-splitting[243].

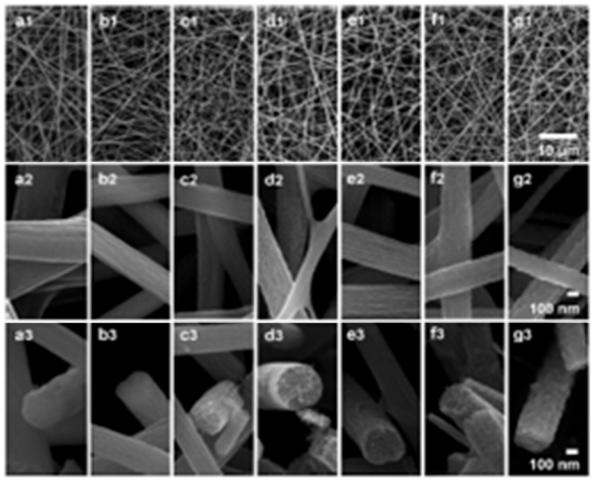

Fig.19 SEM images of (a) as-spun PVP/TiO_2 composite nanofibers and TiO_2 nanofibers after calcination at various temperatures of (b) 300, (c) 400, (d) 450, (e) 500, (f) 600, and (g) 700 °C for 3 h[221].

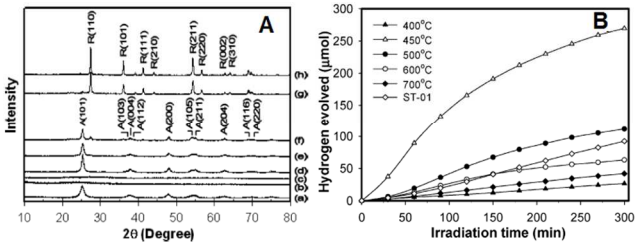

Fig.20 (A) XRD patterns of a: TiO_2-Deggusa (ST-01), b: pre-calcined as-spun NFs, and NFs calcined at c: 300ºC, d: 400ºC, e: 450ºC, f: 500ºC, g: 600ºC and h: 700 °C; lattice planes of A & R represents anatase and rutile phases. (B) The corresponding photocatalytic hydrogen evolution for the TiO_2 fibers calcined at various temperatures, as compared with TiO_2NP powder (Ishihara ST-01)[221].

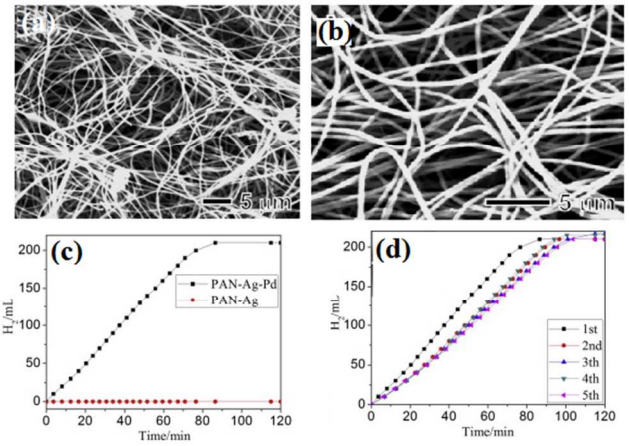

Fig. 21 (a) FESEM images of the PAN/Ag/Pd nanofibers (b) FESEM images of the PAN/Ag/Pd nanofibers after 5th cycle of the catalytic reactions (c) H_2 generation in presence of PAn/Ag/Pd nanofibers and PAN/Ag nanofibers with respect to time, and (d) five cycles of the catalytic reaction is presented[244].

Tong et al. were fabricated the electrospun PAN/Ag/Pd composite fibers, were demonstrated towards their high

performance photocatalytic hydrogen generation[244]. This catalyst material had also proved excellent for recycle stability which is presented in Fig 21. Electrospun nanofibers of PAN/Ag/Pd catalyst were look like network like structures before and after catalytic test as shown in Fig 21 (a & b). The H_2 evolution of PAN/Ag/Pd and PAN/Ag nanofibers with respect to time is presented in Fig 21 (c & d). The amount of H_2 generated from PAN/Ag/Pd nanofibers is much higher than that of the PAN/Ag which is also stable up to 5th cycle. Compound semiconductors provide interesting properties in the enhancement for overall water-splitting in photocatalytic hydrogen generation. *Maeda et al.* reported the highly photoactive catalysts solid solution compound $(Ga_{1-x}Zn_x)(N_{1-x}O_x)$, showed the overall quantum efficiency of about 2.5% under the visible light (420-440 nm) irradiation[245]. The quantum efficiency decreased with increasing wavelength, and it suggested that the longer wavelengths were suitable for the solid solutions for overall water splitting to produce hydrogen. The total production of hydrogen was about 16.2 mmol after irradiation[246]. Recently our group, *Babu et al.* studied MWCNTs doped TiO_2 electrospun hybrid nanostructures for photocatalytic degradation and hydrogen evolution[247]. The doping changed the hydrogen yield and increment in solar to hydrogen conversion efficiency and it led to improve in the charge separation and extending the photoexcitation at the interface of the working electrode and electrolyte of the system. *Choi et al.* prepared directionally aligned NFs consisting three dimensional (3D) spherical TiO_2NPs via electrospinning[248]. The light induced hydrogen productions from Eosin dye sensitization, had improved a factor of 140 in presence of triethanolamine (TEOA) as electron donors. The enhancement in hydrogen generations was because of change in physicochemical properties such as solution change, pH, adsorption range of the dye, BET surface area, diameter of the particle and crystalline nature.

Table 3summarizes the electrospun nanofibers employed for the hydrogen energy generation and showed the hydrogen generation is dependent on surface area, morphology and calcination temperatures.

Table 3 Summary of photocatalytic hydrogen generation based on electrospun NFs produced upto date.

Photocatalyst (Different morphologies)	Light source	Surface area (m^2/g)	Production H_2(μmol/h)	Ref.
TiO_2 (450 °C)	450-W Hg (UV)	56.3	54	[221]
TiO_2 (450 °C)	400-W Hg (UV)	47.75	90	[242]
TiO_2 (500 °C)	>420 nm (visible)	96.3	206	[248]
TiO_2 (500 °C)	450-W Hg (UV)	58.2	19.1	[240]
TiO_2/N_2 (450°C)	150-W Xe (visible)	70	28	[249]
TiO_2/Pt(500 °C)	>420 nm (visible)	96.3	7110	[248]
$TiO_2/SrTiO_3$	400-W Hg (UV)	50.33	330	[242]
$SrTiO_3$ (500 °C)	450-W Hg (UV)	122	81	[250]
TiO_2/CuO (450 °C)	400-W Hg (UV)	108.1	62.7	[177]
TiO_2/SnO_2(450 °C)	400-W Hg (UV)	73.1	200	[243]

6. Fuel cells

Fuel cells are electrochemical devices where energy stored in chemical fuel is converted into electricity in the presence of a metal catalyst. Hydrocarbons such as methanol and renewable fuel sources namely (bio) ethanol were used as fuel source in fuel cells. Among them, direct methanol fuel cell (DMFC) was found to be simple, low cost and low temperature operation and economically viable. Proton exchange membrane fuel cell (PEMFC) and DMFC were being demonstrated for portable applications such as cellular phones, laptops and personal digital assistants (PDAs). The use of high loading of catalysts such as Pt (20-60 wt%) and high cost of the catalyst, limit their potential application commercially. Hence, various carbon materials such as mesocarbon microbeads[251], ordered mesocarbon microbeads, activated carbon NFs (CNFs)[252, 253], graphene[254-256], activated carbon NFs (CNFs) [257, 258] and other carbonaceous materials have been used as supports. Some of the supporting materials tested are shown in Fig. 22.

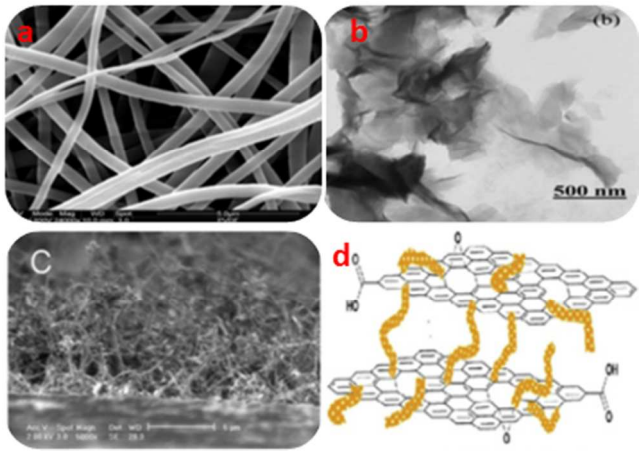

Fig.22 Supporting materials used for fuel cell applications: (a) graphene [256], (b) CNFs, (c) vertically grown CNTs[259], and (d) CNT on graphene[252].

Kim et al. demonstrated an enhancement in electrochemical activity of the Pt nanowire by electrospinning of PVP–Pt composite fibers followed by heat treatment. The physicochemical and electrochemical properties of the Pt nanowires were dependent on heat treatment conditions such as heating rate, temperature, time, and atmosphere. Although higher methanol oxidation rate value of 1.41 mA cm^{-2} was observed for Pt nanowires when compared with commercial Pt black of 1.36 $mAcm^{-2}$, low surface area of 6.2 m^2 g^{-1} were observed for Pt nanowires, which can be improved by stepwise heat treatment[260]. Polyamide composite Pd/PA6 NFs with highly porous structure and excellent mechanical property were fabricated by the combination of electrospinning and an electroless plating approach and tested for electro-oxidation of alcohols in alkaline medium[261]. They observed high current density and low I_b/I_f and the enhanced performance, which was ascribed to the large surface area, reduced diffusion resistance and excellent poisoning tolerance.

6.1 Carbon based NFs

1D material such as CNTs and CNFs are considered to be promising support materials for catalysts in fuel cells, due to their unique structures, highelectronic and thermal conductivities, and good electrochemical stability. Compared with CNTs, carbon NFs are cheap, easy to produce, and different architectures can be prepared. The electrospun CNF due to high porosity and surface area to volume ratio, found to be an alternative choice for Pt catalytic particles and thereby both protons and reactants were accessible for the improved performance. Polyacrylonitrile (PAN) and polyimide (PI) polymers have been widely used as polymer of choice to produce CNF. Researchers have reported polyimide-based CNFs through electrospinning technique followed by subsequent heat treatment process[262, 263].The conductivity of such NFs was much higher than those of other types of CNF mat. They noticed that the conductivity increased with decreasing diameter, which could be attributed to the packing density and diameter of NFs, both these parameters affect the numbers of cross-junctions between NFs per unit volume of the mat[264]. *Park et al*. reported the Pt catalysts utilization can be increased (to 69%) when the catalyst was deposited on electrospun CNF compared to that of 35 % utilization on carbon black Pt/XC-72R[265]. This showed that CNFs were better support materials for Pt catalysts. In another study, the Pt/C supported on the CNFs exhibited higher electrocatalytic activity, more stability, larger exchange current and smaller charge transfer resistance than that on commercial carbon papers. This had been ascribed to the good dispersion of catalyst particles into the CNF mats and thereby led to a small contact resistance between the catalyst particles and the supporting materials[266]. *Li et al.* reported the platinum clusters of 50-200 nm size electrodeposited on the CNF electrodes achieved the catalytic peak current reaching 420 mA mg^{-1}, compared to commercial catalyst 185 mA mg^{-1}. Although the Pt clusters were of relatively larger size, they were favourable to improved performance[267]. Similarly, several researchers electrodeposited, Pt NPs on PAN CNF[268] and gold on PAN CNF[269]. *Guo et al.* noticed the exchange current density upon oxidation of methanol was easier and exchange current density (j_o) for gold NPs on PAN CNF was 2.7 times larger than on pure gold electrodes[269]. *Xuyen et al.* immobilized Pt precursors through nucleation process on polyimide NFs and subsequent heating produced Pt loaded PI based CNF as electrodes for fuel cell[270]. Recently, researchers reported the 1-aminopyrene functionalized (APF) Pt NPs formed on CNF through polyol process which tend to form NPs with a smaller size and better distribution compared with conventional and acid treated catalysts. Also, these APF carbon NFs possessed excellent properties of high active surface area, improved performance toward the electrocatalytic oxidation of methanol, and relatively good long-term stability[271].

Pt/CNF nanocomposites were produced by the reduction of hexachloroplatinic acid (H_2PtCl_6) using formic acid (HCOOH) in aqueous solution containing CNF by *Wang et al*[272]. These Pt/CNF nanocomposites showed higher electrocatalytic activity toward methanol oxidation compared with commercial E-tek Pt/C catalyst, which are presented in Fig. 23. Several researchers reported the combination of semiconducting oxide materials with catalytically active noble metals like Pd/TiO_2, Pt/WO_3 for not only to act as support material but also to achieve enhanced electrocatalytic properties[273-275]. Several techniques such as electroless plating, galvanic replacement method and polyol process were employed to deposit the metals on the oxide materials. Pd is found to be a promising substitute for Pt in alcohol oxidation reaction, due to their outstanding electrocatalytic activity and more abundant in nature. *Su et al.* employed electroless - plating of Pd on the electrospun TiO_2NFs. They fabricated Pd/TiO_2NFs showing excellent electro oxidation behaviour towards glycerol in alkaline medium[273]. *Zhao et al.* fabricated Pt nanospheres and Pt nanocubes on electrospun WO_3 and observed that Pt nanocubes were much more active than Pt nanospheres, and also the activity of Pt supported onWO_3NFs (Fig.24) was higher than that supported on commercial WO_3[274].

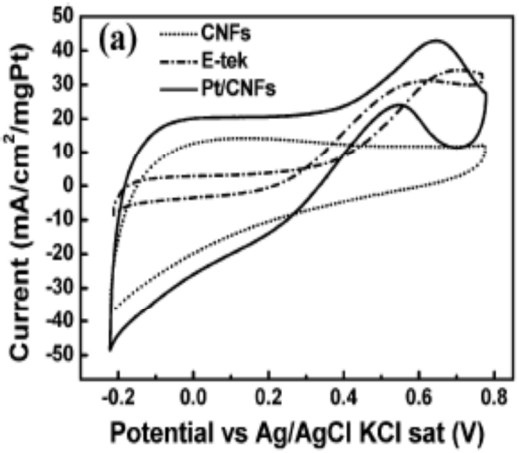

Fig. 23 Cyclic voltammetry of E-tek, Pt/CNFs and CNF mat without Pt loading[273].

Pt NPs and nanowires decorated on the electrospun anatase NFs were proved to be effective electrocatalysts for direct methanol oxidation[275]. Similarly, few researchers attempted to use CNF as support for the alloy deposition (like Pt–Pd)[276]and hetero-polyacids(HPA)[277].Among the various tested compositions of alloys, nanocomposites with $Pt_{50}Pd_{50}$/CNFs had the best electrocatalytic activity by mass toward the oxygen reduction. In an another study, HPA were incorporated into the PAN CNF to increase the electrical conductivity of the CNFs[277]. The increasing HPA content had increased both the electrical conductivity and surface area of CNFs. PAN CNF supported Fe/Co/Ni ternary alloy NPs were alsoprepared by using the electrospinning technique for potential fuel cell application[278]. *Seki et al.* shown the electrical conductivity of the CNF can be further increased by applying ion-beam irradiation in which irradiation had resulted in structural change to more ordered graphitic structures[279]. *Chang et al*. fabricated graphene-modified CNF mats (GCNFs) by thermal treatment of electrospun PAN NFs decorated with graphene oxide[280]. The Pt particles were then adsorbed on the GCNF by using formaldehyde vapor and H_2PtCl_6Æ$_6H_2O$. The resulting Pt–GCNFs electrode exhibited excellent electrocatalytic activity and long-term stability toward methanol oxidation, which had shown that they can be used as the anode in DMFCs for long-term applications. Further, the electrode achieved high conductivity of about 65 S cm^{-1} with good flexibility[280].

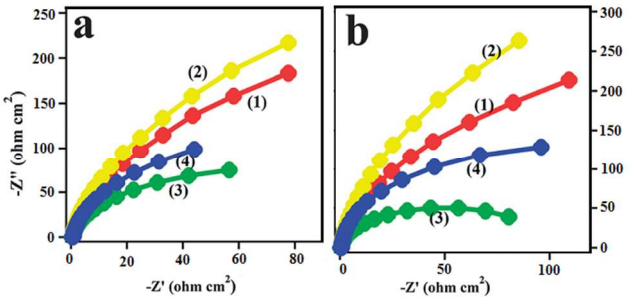

Fig. 24 Impedance spectra of the catalysts in 1M CH_3OH-1M H_2SO_4 at (a) 0.4 V and b) 0.5 V. In the figure (1) Pt nanospheres-WO_3nanofibers (2) Pt nanospheres- commercial WO_3 (3)Pt nanocubes- WO_3 nanofibers and (4) Pt nanocubes-commercial WO_3 [274].

Electroactive bacteria have been explored as electrocatalyst to facilitate the anodic oxidation in microbial fuel cells (MFC). *Chen et al.* have reported the fabrication of layered architecture CNF by layer-by-layer (LBL) electrospinning of PAN onto cellulose paper and subsequent carbonization. This layered CNF had shown to be a promising material for continuous layered biofilms growth and generated high current density. The current density observed for conventional CNF, two dimensional polyacrylonitrile CNF and layered CNF were 1.21, 0.53, 0.17 and 2.0 mA. cm^{-2}, respectively[281]. Similarly, the same group achieved the highest anode current density of upto 30 A m^{-2} for the electroactive microbial fuel cell. The current density for the cell was higher when poly(acrylonitrile-co-itaconic acid-co-butyl acrylate) was used as a precursor during gas-assisted electrospinning in comparison of pure PAN as precursor and solution blowing[282]. This promises NFs as a potential electroactive biofilm material for the sustainable energy supply and handling. *Ghasemi et al*. have tested chemically and physically activated electrospun CNFs (ACNFs) in an MFC and compared their performance with that of conventional carbon paper. The chemically activated CNFs with 8 M KOH exhibited better oxygen reduction reaction (ORR) activity and generated 78% more power than that both of the physically activated ACNFs and conventional carbon paper[283]. *Zhang et al.* employed dip coating method to functionalize PAN CNF surfaces by carbon or silica NPs for MFC application. Further, CNF with higher surface roughness were achieved by optimization of furfuryl alcohol (FFA) concentration and subsequent heating produced carbon NPs (CB) at the fiber surface. The electrical conductivity of such PAN CNF decorated with carbon and PAN + CB with FFA treatment was 126, 290 S/m, respectively[284].

A new class of CNFs, Fe containing carbon NFs (Hb-CNFs) were fabricated by electrospinning of hemoglobin (Hb) and polyacrylonitrile followed by calcinations. The Hb-CNFs glassy carbon electrodes was tested for the amperometric detection of H_2O_2 and they exhibited a faster response, high sensitivity, excellent reproducibility, good selectivity and wide dynamic range with good limit of detection[285]. Electrospun PCL NFs containing Ag has also been tested as electrocatalytic anode membranes for the oxidation of glucose in an alkaline fuel cell[286]. The ENMs fabricated from electrospun NFs composed of sulfonated poly(arylene ether sulfone) with sulfonated polyhedral oligomeric silsesquioxane (sPOSS) as a proton conductivity enhancer had showed 2.4 times higher protonic conductivity than nafion membrane[287].

6.3 Solid oxide fuel cells (SOFC) based on electrospun metal oxide

Electrospun NFs have also been explored as electrode materials in SOFC applications. Electrospinning of lanthanum strontium cobalt ferrite (LSCF) NFs was carried out and used as the cathode of an intermediate-temperature SOFC[288]. The electrochemical performance of the fuel cell with LSCF NF as cathode exhibited a power density of 0.90Wcm^{-2} at 1.9 A cm^{-2} at 750 ^oC, which was further improved by infiltration of 20 wt% of gadolinia-doped ceria (GDC) into the LSCF NF cathode. It showed a power density of 1.07 W cm^{-2} at 1.9 A cm^{-2} at 750 ^oC. This improved performance had been ascribed to (i) high porosity, (ii) high percolation, (iii) continuous pathway for charge transport, (iv) excellent scaffold for infiltration and (v) good thermal stability of the NFs.$Ba_{0.5}Sr_{0.5}Fe_{0.8}Cu_{0.2}O_{3-\delta}$ (BSCF) NFs with high porosity and surface area have been fabricated and compared with powder form for low-temperature SOFC[289]. The area specific resistance (ASR) of the BSCF NF cathode was 0.094 Ωcm^2 at 600 ^oC, whereas that of the BSCF powder cathode was 0.468 Ωcm^2, which suggested that reduction of the interfacial resistance was important for improving the performance of the cell. Yttria stabilized Zirconia (YSZ) NFs were fabricated by electrospinning and the fiber surfaces were coated with a layer of Ni surfaces by electroless plating method for SOFC[165]. The peak power density of fiber-derived anode cell was found to be twice when compared with the powder-derived anode. This was attributed to the well-structured and interconnected fibers in the former case. Metal oxides have been explored as low cost alternative catalyst for methanol oxidation. *Zhang et al.* prepared PdO-Co_3O_4NF composite with good electrocatalytic activity toward methanol when Nafion/PdO-Co_3O_4/GCE was used as electrodes[15]. Similarly, *Al-Enizi et al.* reported nanocomposite made of electrospun cobalt oxide and CNFs as electrode material for fuel cell application in which the enhanced electrochemical activity was shown by well dispersed cobalt oxide NP within the frame work of CNF[290].

6.4 Electrospun Nanofibrous Membrane

In the case of PEMFC, the handling of hydrogen as fuel is critical. In order to achieve efficient proton conduction, the water management of PEM is very crucial. Although varieties of solutions were proposed for this issue, DMFC was studied as an alternative to PEMFC in portable applications. Currently, the DMFC efficiency that has been achieved upto 40%.Hence researchers are focusing on the development of efficient membrane that will prohibit the methanol crossover. Various contributing factors include methanol concentration, PEM material, thickness of PEM, operating current density, pressure and temperature. Nafion is one of the most widely studied polymers as membranes in fuel cell applications. Several researchers attempted to modify the Nafion with NPs, reinforcement with other polymers or interesting nanostructures to reduce methanol crossover and swelling to increase the protonic conductivity or increase mechanical property of the resulting membranes. ENMs were known to contribute additional morphology effect for the resulting membranes. Electrospinning of PVA and poly(4-styrenesulfonic acid) polymers with fiber

diameters ranged from 176 to 766 nm and subsequently heat treated to achieve water stable PEM membranes[291]. *Choi et al.* fabricated perfluorosulfonic acid (PFSA) NF membranes in presence of PEO as a carrier polymer with Norland optical adhesive. The fibers were cross linked using adhesive chemistry and PEO was subsequently removed. They reported NFs of higher proton conductivities (0.16 S/cm) and improved mechanical properties when compared to that of commercial Nafion 212 membrane (0.048S/cm) in film form[292]. Several researchers have used PVP and /or PS,PEO or PVA as the carrier polymers[293, 294]. *Ballengee et al*. used carrier polymer of different molecular weight with low concentration (1-2 wt %) and observed various morphologies such as bead-on-fiber structures and ribbon like morphology depending on the polymer molecular weight and electrospinning conditions such as humidity, voltage and flow rate[295]. Some groups fabricated a composite membrane from electrospun poly(ether sulfone) (PES)[296, 297]or poly(vinylidene fluoride)PVDF NFs[298], the pores being filled with nafion matrix. It resulted in higher proton to methanol selectivity and single cell DMFC performance for composite membranes than Nafion112 and Nafion117 membranes. *Tamura et al.* shown that the PI within NFs were significantly oriented in composite membrane and the resulting aligned nanostructures were found to possess high proton conductivity and low gas permeability into the fuel for PEMFC(Fig. 25)[258].

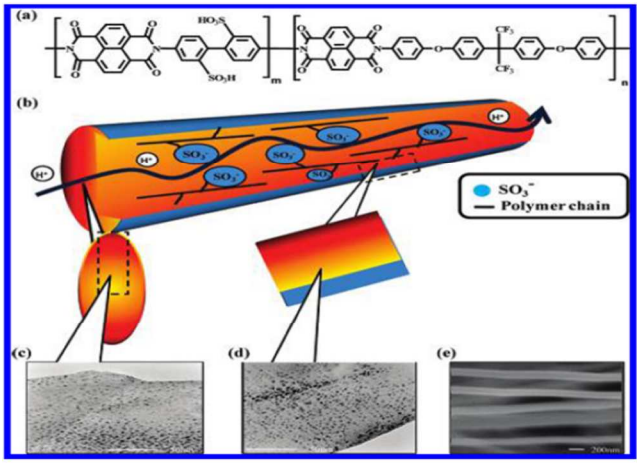

Fig. 25(a) Chemical structure of random copolyimide (1,4,5,8-Naphthalene tetracarboxylic dianhydride-4,4'-Diamino-biphenyl 2, 2'-disulfonic acid-*random* - 2, 2- Bis [4-(4-aminophenoxy) phenyl]-hexafluoropropane, abbreviated as NTDA-BDSA-r-APPF) (b) Schematic representation of sulfonated copolyimide NF. (c) TEM image of cross-sectional aligned NF in radial direction. (d) TEM image of cross-sectional aligned NF in axial direction. (e) SEM image of aligned NF electrospun on special designed collector[258].

The same group reported the aligned PI NFs, they observedthe parallel conductivity was higher than the perpendicular conductivity[299]. *Subianto et al.* studied the effect of side-chain length (short side chain (SSC) and long side chain (Nafion)) of perfluorosulfonic acid (PFSA) monomers on the conducting properties of NFs. In the case of SSC PFSA/carrier polymer, lower average fiber diameter and a markedly narrower fiber size distribution were observed due to enhanced inter-chain interactions. The proton conductivity of NF mats of SSC PFSA was 102 mS cm^{-1} when compared to Nafion of 58 mS cm^{-1}at 80°C[300]. *Ballengee et al*. fabricated two structures such as (i) nafion reinforced by a poly(phenyl sulfone) NF network (structure 1) and (ii) Nafion NFs embedded in poly (phenyl sulfone) NF (structure 2), by side-by-side dual spinneret approach in simple electrospinning process for PEMFC. They compared structure 2 with structure 1 (Fig. 26). Structure 2 exhibited very low water swelling and better mechanical properties when compared to structure 1[257].Similarly, *Liu et al*. reported electrospun nanofibrous membranes made of hydrophilic sulfonated poly(fluorenyl ether ketone) (SPFEK) NFs and hydrophobic beaded PES NFs by using a co-electrospinning method followed by removal of PES by dissolving process. Finally, in-situ gap filling was achieved by electrostatic layer by layer (LBL) self-assembly of anionic and cationic polyelectrolyte polymers. The resulting membrane possessed excellent oxidative stability, high proton conductivity of 0.056–0.061 S cm^{-1} at 30–80 °C, and power density of 0.28Wcm^{-2} at 80 °C. The fabricated membranes achieved a facile proton conducting pathway with activation energy (E_a) of 1.30 kJ mol^{-1}, which was very low value, when compared to the value of 8.14 kJ mol^{-1} for Nafion[301].

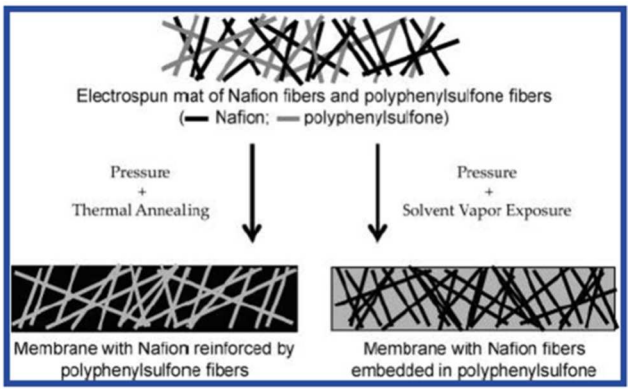

Fig. 26 Creating two NF-composite Nafion/poly(phenyl sulfone) membrane structures from the same dual fiber electrospun mat[257].

Yao et al. fabricated a hybrid membranes consisted of superacidic electrospun sulfated zirconia (S-ZrO_2) fibers to recast Nafion for PEMFC. The S-ZrO_2 was fabricated from the electrospinning of Zr precursor in presence of carrier polymer, followed by sulfonation and calcinations (Fig. 27(a)). The solid S-ZrO_2 fibers helped to gather a large amount of protogenic groups of Nafion into the interfaces, which favoured for the continuous ionic pathways for effective proton transport in the membranes (Fig. 27(b)).High proton conductivities of 3.1×10^{-1}S $\cdot cm^{-1}$ for hybrid membranes by selectively adjusting the fiber diameter and fiber volume fraction were achieved, when compared to the Nafion of 9.1×10^{-2} S cm^{-1}[302].

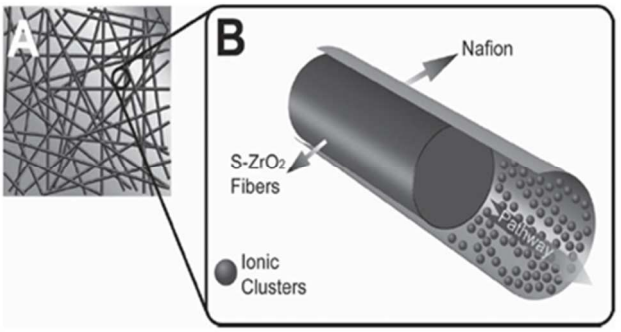

Fig. 27 Schematic diagrams of (a) S-ZrO_2 fiber-Nafion hybrid membrane, and (b) the interface between S-ZrO_2 fiber and the Nafion matrix with ionic clusters aggregating on the S-ZrO_2 fiber-Nafion interface[302].

In another study, the same group reported the fabrication of hybrid membrane, by replacing S-ZrO_2 with sulfonated polystyrene (S-PS) electrospun fibers into Nafion. Similar to S-ZrO_2, the S-PS favored for the large amount of sulfonic acid groups in Nafion aggregated onto the interfaces between S-PS fibers and the ionomer matrix, and thereby formed the continuous pathways for facile proton transport. A high proton conductivity of $1.8X10^{-1}$ S cm^{-1} was observed at 80 °C and 100% RH for the fiber diameter of 0.98 μm[303]. Electrospun NFs are promising materials in SOFC, which provide high power density due to high porosity, high percolation, continuous pathway for charge transport, excellent scaffold for infiltration and good thermal stability. The materials can be fabricated in large scale and tested for their performance in future as the large scale production of NFs through electrospinning. Several studies have shown that electrospun NFs were the best choice to use as support materials for the purpose of catalysts anchoring in fuel cell electrodes and as PEM, which has to be fabricated and tested in large scale.

7. Future perspectives

Electrospun nanostructures of various metal oxides and composite with well controllable structures were shown to be as promising materials for energy efficient devices and environmental applications. In this review, several formulations of NF by one step electrospinning with different spinneret (dual spinnerets, core–shell spinneret), collector with post-modification/treatment were discussed for synthesizing different hierarchical NFs with superior functional properties. The morphology and diameters of the NFs are optimized by changing electrospinning parameters which would be more beneficial to retard photo induced electron and hole recombinations. Highly crystalline NF morphology (random, hollow, mesoporous structures) are widely used as low cost photoanode and counter electrodes in DSSCs and QDSSCs which observed significant increase in energy conversion efficiency when compared to other nanomaterial synthesis and growth process. Synthesized electropsun nanostructured fibers exhibited improved photocatalytic performance in water splitting compared to other nanostructures produced from other conventional methods. The photocatalytic properties including photocurrent with respect to potential is not only affected the system resistance but also strongly influenced the carrier separation, recombination, and transfer process through variation in the band structure of the nanostructures. This review provides a critical insight for the different designs of nanostructured architectures for hydrogen generation through direct photocatalytic water splitting under UV and Visible light irradiation.

Electrospun NFs already proven that they are potential for anchoring of catalysts in fuel cell electrodes. The contribution of NFs in enhancement of conductivity, performance dependent on morphologies, and lowering activation energy is also proven to use in PEMFC applications. Electrospun NFs are promising materials in SOFC, which provide high power density due to high porosity, high percolation, continuous pathway for charge transport, excellent scaffold for infiltration and good thermal stability. The materials can be fabricated in large scale and tested for their performance in future large scale production of NFs. Several studies have shown that electrospun NFs are the best choice to use as support materials for the purpose of catalysts anchoring in fuel cell electrodes and as PEM.

8. Summary and outlook

In summary, electrospun 1DNFs are versatile in photon absorption and carrier separation/collection due to their large surface area and anisotropic properties, which could enhance the solar energy harvesting efficiencies. In addition NFs by electrospining showed enhanced crystallinity, surface area and photocatalytic activity for hydrogen evolution compared to the NFs produced by other synthesis methods. The 1D nanotubular structures demonstrated their apparent advantage for the photocatalytic hydrogen generation over NPs which was because of the favorable electron transfer and reduced recombination of electron-hole pairs. Modification of 1D NFs into hierarchical nanostructures or hybrid structures (core–shell, 0D and 1D) with supporting materials can further increase the light absorbance and/or improve the carrier collection efficiency. Therefore, by using band gap tuning and nanostructure design, 1D NFs hold the potential for the cost effective and high efficiency PV and PEC solar cells for the hydrogen energy generation. Over and above, the electronic structure of semiconductor plays a key role in photocatalytic water-splitting, as the photogenerated e^-/h^+ can recombine in very short time by releasing energy in the form of photons on surface of the photocatalyst. The reduction and oxidation reactions are the two necessary mechanisms in photocatalytic hydrogen generation. The surface adsorption and photocatalytic activity performance could be enhanced by reducing dimensionality which can facilitates more reactive surface area in nanostructured catalysts. For the efficient hydrogen production, the CB level of the catalyst should be more negative than hydrogen production level, while the VB should be more positive than water oxidation level for oxygen from watersplitting. Theoretically, the catalysts should fulfil these conditions for the generation of hydrogen. High chemical stability and long lifetime of e^-/h^+pairs are the key parameters for leading strong photocatalytic hydrogen generation. However, the solar to hydrogen conversion by water splitting is very limited, there are few inhibiting and challenging factors such as (a) recombination: the electrons from CB can recombine with holes in VB within short time and release energy in the form of photons, (b) backward reaction: the decomposition of H_2O into H_2 and O_2 is an energy increasing process, so the reaction proceeds to form H_2O from H_2 and O_2 as backward reaction, (c)

effective utilization of visible light: nearly 50% of the solar energy contribution is from the visible light, but the most of our the present technology is depending on large band gap semiconducting catalysts and therefore visible light utilization is also one of the important issues for solar photocatalytic hydrogen energy generation. In order to overcome these challenges, and produce efficient hydrogen one can need to modify the semiconductors with the following the steps as: addition of electron donors (hole scaveengers), addition of carbonate salts, noble metal loading, metal ion doping, anion doping, dye sensitization, composite semiconductors, metal ion implantation and improvement in surface area, thereby reduction in band gap energy[228]. Due to the strict confinement of band energy alignment with the water-splitting potential and the stability in electrolyte solutions, there is still a huge demand to explore more 1D based hierarchical nanostructured designs and fabrication to further increase the solar hydrogen production efficiency.

Electrospun NFs are shown to be an alternative choice of materials for anchoring of catalysts in fuel cell electrodes, as membranes in PEMFC and SOFC. Some of the issues to be solved for commercial application of NFs for fuel cell applications are (i) achievement of uniform fiber diameters of below 50 nm, (ii) green processing of nanofibrous membranes and catalysts using eco-friendly medium, and (iii) large scale production. Although better performance shown by NFs as catalyst electrodes and membrane is encouraging their use in fuel cell applications, but the cost has to be reduced for their potential exploration in commercial application.

9. Acknowledgements

This work was supported by grants from the Russian Science Foundation to SIA. Author VJB acknowledge The Scientific & Technological Research Council of Turkey (TUBITAK) (TUBITAK-BIDEB 2221, Fellowships for visiting scientists and scientists on sabbatical leave) for their fellowship.

10. Notes

[a]*Center for Nanofibers and Nanotechnology, National University of Singapore, 117576,Singapore.*
[b]*Environmental & Water Technology, Centre of Innovation, Ngee Ann Polytechnic, Singapore*
[c]*Department of Mechanical Engineering, National University of Singapore, 117576,Singapore.*
[d]*UNAM-National Nanotechnology Research Center, Bilkent University, Ankara-06800, Turkey.*
[e]*Institute of Plant Physiology, Russian Academy of Sciences, Botanicheskaya Street 35, Moscow 127276, Russia*
[f]*Institute of Basic Biological Problems, Russian Academy of Sciences, Pushchino, Moscow Region 142290, Russia.*
Corresponding author email address: seeram@nus.edu.sg; sureshinphy@yahoo.com; sundaram1304@gmail.com; sundarnus1@gmail.com; vjbabu2002@gmail.com

11. Reference

1. J. A. Turner, *Science*, 1999, **285**, 687-689.
2. N. S. Lewis, *MRS Bulletin*, 2007, **32**, 808-820.
3. V. S. Arunachalam and E. L. Fleischer, *MRS Bulletin*, 2008, **33**, 264 - 288.
4. *International Energy Agency*, http://www.iea.org/aboutus/faqs/renewableenergy/.
5. Y. Gu, I. L. Kuskovsky, M. Yin, S. O'Brien and G. F. Neumark, *Appl.Phys.Lett.*, 2004, **85**, 3833-3835.
6. A. Gasparotto, D. Barreca, C. Maccato and E. Tondello, *Nanoscale*, 2012, **4**, 2813-2825.
7. Y. Yin and D. Talapin, *Chem.Soc.Rev.*, 2013, **42**, 2484-2487.
8. V. J. Babu, S. Vempati, S. Sundarrajan, M. Sireesha and S. Ramakrishna, *Solar Energy*, 2013, **106**, 1-22.
9. Q. Zhang, E. Uchaker, S. L. Candelaria and G. Cao, *Chem.Soc.Rev*, 2013, **42**, 3127-3171.
10. Y. Ye, C. Jo, I. Jeong and J. Lee, *Nanoscale*, 2013, **5**, 4584-4605
11. Y. Li and J. Z. Zhang, *Lasers & Photonics Rev.*, 2010, **4**, 517-528.
12. H. K. Raut, V. A. Ganesh, A. S. Nair and S. Ramakrishna, *Energy Environ. Sci.,*, 2011, **4**, 3779-3804.
13. N. Nuraje, W. S. Khan, Y. Lei, M. Ceylan and R. Asmatulu, *J.Mater.Chem.A*, 2013, **1**, 1929-1946
14. M. M. Khin, A. S. Nair, V. J. Babu, R. Murugan and S. Ramakrishna, *Energy Environ. Sci.,*, 2012, **5**, 8075-8109.
15. Y. Zhang, Y. Wang, J. Jia and J. Wang, *Int.J.Hydrogen Energy*, 2012, **37**, 17947-17953.
16. L.-C. Cheng, X. Jiang, J. Wang, C. Chen and R.-S. Liu, *Nanoscale*, 2013, **5**, 3547-3569.
17. C. Zhao, A. Tan, G. Pastorin and H. K. Ho, *Biotechnol.Adv.*, 2013, **31**, 654-668.
18. A. Dhayal Raj, P. Suresh Kumar, Q. Yang and D. Mangalaraj, *Physica E: Low-dimensional Systems and Nanostructures*, 2012, **44**, 1490-1494.
19. P. S. Kumar, A. D. Raj, D. Mangalaraj and D. Nataraj, *Applied Surface Science*, 2008, **255**, 2382-2387.
20. A. Joseph Nathanael, D. Mangalaraj, P. C. Chen and N. Ponpandian, *Composites Science and Technology*, 2010, **70**, 419-426.
21. Y. Liu, J. Goebl and a. Y. Yin, *Chem.Soc.Rev*, 2013, **42**, 2610-2653.
22. B. B. Lakshmi, P. K. Dorhout and C. R. Martin, *Chemistry of Materials*, 1997, **9**, 857-862.
23. P. Suresh Kumar, J. Sundaramurthy, D. Mangalaraj, D. Nataraj, D. Rajarathnam and M. P. Srinivasan, *Journal of Colloid and Interface Science*, 2011, **363**, 51-58.
24. Y. Li, X.-Y. Yang, Y. Feng, Z.-Y. Yuan and B.-L. Su, *Critical Reviews in Solid State and Materials Sciences*, 2012, **37**, 1-74.
25. C. Zhang, Y. Yan, Y. S. Zhao and J. Yao, *Annu. Rep. Prog. Chem., Sect. C: Phys. Chem.*, 2013, **109**, 211-239
26. C. N. R. Rao, S. R. C. Vivekchand, K. Biswas and A. Govindaraj, *Dalton Trans.*, 2007, 3728-3749
27. S. Kalluri, K. H. Seng, Z. Guo, H. K. Liu and S. X. Dou, *RSC Adv*, 2013, **3**, 25576-25601.
28. B. Ding, M. Wang, X. Wang, J. Yu and G. Sun, *Mater.Today*, 2010, **13**, 16-27.
29. H. Ma, C. Burger, B. S. Hsiao and B. Chu, *J.Mater.Chem.*, 2011, **21**, 7507-7510.
30. J. Xie, M. R. MacEwan, A. G. Schwartz and Y. Xia, *Nanoscale*, 2010, **2**, 35-44.
31. *BCC Research*, 2010, Nanofibers: Technologies and Developing Markets, Report Code: NAN043B.
32. C. J. Luo, S. D. Stoyanov, E. Stride, E. Pelan and M. Edirisinghe, *Chem.Soc.Rev*, 2012, **41**, 4708-4735.
33. R. Sahay, P. S. Kumar, V. Aravindan, J. Sundaramurthy, W. C. Ling, S. G. Mhaisalkar, S. Ramakrishna and S. Madhavi, *J. Phys. Chem. C*, 2012, **116**, 18087–18092.
34. T. Maiyalagan, J. Sundaramurthy, P. S. Kumar, P. Kannan, M. Opallo and S. Ramakrishna, *Analyst*, 2013, **138**, 1779-1786
35. P. S. Kumar, V. Aravindan, J. Sundaramurthy, V. Thavasi, S. G. Mhaisalkar, S. Ramakrishna and S. Madhavi, *RSC Adv.*, 2012, **2**, 7983-7987.
36. V. Aravindan, P. S. Kumar, J. Sundaramurthy, W. C. Ling, S. Ramakrishna and S. Madhavi, *J.Power Sources*, 2013, **227**, 284-290.
37. C. T. Cherian, J. Sundaramurthy, M. V. Reddy, P. S. Kumar, K. Mani, D. Pliszka, C. H. Sow, S. Ramakrishna and B. V. R. Chowdari, *ACS Appl. Mater. Interfaces*, 2013, **5**, 9957–9963.

38. S. Jayaraman, V. Aravindan, P. S. Kumar, W. C. Ling, S. Ramakrishna and S. Madhavi, *ACS Appl. Mater. Interfaces*, 2014, **DOI: 10.1021/am501464d**.
39. S. Jayaraman, V. Aravindan, P. S. Kumar, W. C. Ling, S. Ramakrishna and S. Madhavi, *Chem. Commun*, 2013, **49**, 6677-6679.
40. V. Aravindana, J. Sundaramurthy, E. N. Kumar, P. S. Kumar, W. C. Ling, R. v. Hagen, S. Mathur, S. Ramakrishna and S. Madhavi, *Electrochim.Acta*, 2014, **121**, 109–115.
41. X. Zhang, P. S. Kumar, V. Aravindan, H. H. Liu, J. Sundaramurthy, S. G. Mhaisalkar, H. M. Duong, S. Ramakrishna and S. Madhavi, *J.Phys.Chem.C*, 2012, **116**, 14780–14788.
42. R. Sahay, P. S. Kumar, R. Sridhar, J. Sundaramurthy, J. Venugopal, S. G. Mhaisalkar and S. Ramakrishna, *Journal of Materials Chemistry*, 2012, **22**, 12953-12971.
43. Z. M. Huang, Y. Z. Zhang, M. Kotaki and S. Ramakrishna, *Comp. Sci.Technol.*, 2003, **63**, 2223–2253.
44. P. S. Kumar, R. Sahay, V. Aravindan, J. Sundaramurthy, W. C. Ling, V. Thavasi, S. G. Mhaisalkar, S. Madhavi and S. Ramakrishna, *J.Phys. D:*, 2012, **45**, 265302.
45. R. Ramaseshan, S. Sundarrajan, R. Jose and S. Ramakrishna, *J.Appl.Phys.*, 207, **102**, 111101.
46. W. E. Teo and S. Ramakrishna, *Nanotechnology*, 2006, **17**, R89-R106.
47. V. J. Babu, A. S. Nair, Z. Peining and S. Ramakrishna, *Mater.lett*, 2011, **65**, 3064-3068.
48. X. Zhang, V. Aravindan, P. S. Kumar, H. Liu, J. Sundaramurthy, S. Ramakrishna and S. Madhavi, *Nanoscale*, 2013, **5**, 5973-5980.
49. J. Sundaramurthy, V. Aravindan, P. S. Kumar, W. C. Ling, S. Ramakrishna and S. Madhavi, *Chem. Commun*, 2013, **49**, 6677-6679.
50. S. Ramakrishna, K. Fujihara, W.-E. Teo, T.-C. Lim and Z. Ma, *World Scintific* 2005, ISBN: 978-981-256-415-3
51. D.-G. Yu, Y. Xu, Z. Li, L.-P. Du, B.-G. Zhao and X. Wang, *Journal of Nanomaterials*, 2014, http://dx.doi.org/10.1155/2014/967295.
52. P. Raghavan, D.-H. Lim, J.-H. Ahn, C. Nah, D. C. Sherrington, H.-S. Ryu and H.-J. Ahn, *Reactive and Funct.Poly.*, 2012, **72**, 915–930.
53. D. H. Reneker and A. L. Yarin, *Polymer*, 2008, **49**, 2387–2425.
54. J. G. Hardy, L. M. Romer and T R Scheibel, *Polymer*, 2008, **49**, 4309–4327.
55. B. Dong, O. Arnoult, M. E. Smith and G. E. Wnek, *Macromol.Rapid Commun.,*, 2009, **30**, 539–542.
56. K. Ohkawa, D. I. Cha, H. Kim, A. Nishida and H. Yamamoto, *Macromol. Rapid Commun.,*, 2004, **25**, 1600–1605.
57. S. Ramakrishna, R. Jose, P. S. Archana, A. S. Nair, R. Balamurugan, J. Venugopal and W. E. Teo, *J. Mater. Sci.,*, 2010, **45**, 6283–6312.
58. P. V. Kamat, *J. Phys. Chem. C,*, 2007, **111**, 2834–2860.
59. K. W. J. Barnham, M. Mazzer and B. Clive, *Nature Mater.*, 2006, **5**, 161-164.
60. B. O'Regan and M. Gratzel, *Nature*, 1991, **353**, 737-740.
61. A. Yella, H.-W. Lee, H. N. Tsao, C. Yi, A. K. Chandiran, M. K. Nazeeruddin, E. W.-G. Diau, C.-Y. Yeh, S. M. Zakeeruddin and M. Grätzel, *Science*, 2011, **334**, 629-634.
62. H. Sun, Y. Luo, Y. Zhang, D. Li, Z. Yu, K. Li and Q. Meng, *J.Phys.Chem.C*, 2010, **114**, 11673–11679.
63. B. Lee, D. B. Buchholz, P. Guo, D.-K. Hwang and R. P. H. Chang, *J.Phys.Chem.C*, 2011, **115**, 9787–9796.
64. R. D. McConnell, *Renew.Sustain.Energ.Rev*, 2002, **6**, 271-293.
65. L. M. Peter, *Phys.Chem.Chem.Phys.*, 2007, **9**, 2630-2642
66. V. Thavasi, G. Singh and S. Ramakrishna, *Energyn & Environ.Sci*, 2008, **1**, 205-221
67. S.-J. Seo, S.-H. Yun, J.-J. Woo, D.-W. Park, M.-S. Kang, A. Hinsch and S.-H. Moon, *Electrochem.Commun.*, 2011, **13**, 1391–1394.
68. A. S. Nair, Z. Peining, V. J. Babu, Y. Shengyuan and S. Ramakrishna, *Phys.Chem.Chem.Phys.*, 2011, **13**, 21248-21261
69. B. H. Lee, M. Y. Song, S.-Y. Jang, S. M. Jo, S.-Y. Kwak and D. Y. Kim, *The Journal of Physical Chemistry C*, 2009, **113**, 21453-21457.
70. Y. P. Lin, Y. Y. Chen, Y. C. Lee and Y. W. Chen-Yang, *The Journal of Physical Chemistry C*, 2012, **116**, 13003-13012.
71. K. Saha, S. S. Agasti, C. Kim, X. Li and V. M. Rotello, *Chemical Reviews*, 2012, **112**, 2739-2779.
72. M. Y. Song, Y. R. Ahn, S. M. Jo, D. Y. Kim and J.-P. Ahn, *Appl.Phys.Lett.*, 2005, **87**, 113113
73. P. S. Kumar, S. A. S. Nizar, J. Sundaramurthy, P. Ragupathy, V. Thavasi, S. G. Mhaisalkar and S. Ramakrishna, *Journal of Materials Chemistry*, 2011, **21**, 9784-9790.
74. Z. Peining, A. S. Nair, Y. Shengyuan, P. Shengjied, N. K. Elumalai and S. Ramakrishna, *J.Photochem.Photobiol. A*, 2012, **231**, 9-18.
75. G. S. Anjusree, A. Bhupathi, A. Balakrishnan, S. Vadukumpully, K. R. V. Subramanian, N. Sivakumar, S. Ramakrishna, S. V. Nair and A. S. Nair, *RSC Adv.*, 2013, **3**, 16720-16727.
76. L. Yang and W. W.-F. Leung, *Advanced Materials*, 2011, **23**, 4559-4562.
77. A. S. Nair, R. Jose, Y. Shengyuan and S. Ramakrishna, *Journal of Colloid and Interface Science*, 2011, **353**, 39-45.
78. A. S. Nair, P. Zhu, V. J. Babu, S. Yang, T. Krishnamoorthy, R. Murugan, S. Peng and S. Ramakrishna, *Langmuir*, 2012, **28**, 6202–6206.
79. H. Krysova, J. Trckova-Barakova, J. Prochazka, A. Zukal, J. Maixner and L. Kavan, *Catal.Today*, 2014, **230**, 234–239.
80. Z. Peining, A. S. Nair, P. Shengjie, Y. Shengyuan and S. Ramakrishna, *ACS Appl. Mater. Interfaces*, 2012, **4**, 581-585.
81. Y. Li, D.-K. Lee, J. Y. Kim, B. S. Kim, N.-G. Park, K. Kim, J.-H. Shin, I.-S. Choi and M. J. Ko, *Energy Environ. Sci.,*, 2012, **5**, 8950-8957
82. X. Zhang, V. Thavasi, S. G. Mhaisalkar and S. Ramakrishna, *Nanoscale*, 2012, **4**, 1707-1716.
83. E. M. Jin, J.-Y. Park, X. G. Zhao, I.-H. Lee, S. M. Jeong and H.-B. Gu, *Mater.lett*, 2014, **126**, 281–284.
84. P. Du, L. Song, J. Xiong, N. Li, Z. Xi, L. Wang, D. Jin, S. Guo and Y. Yuan, *Electrochimica Acta*, 2012, **78**, 392-397.
85. D. Hwang, S. M. Jo, D. Y. Kim, V. Armel, D. R. MacFarlane and S.-Y. Jang, *ACS Applied Materials & Interfaces*, 2011, **3**, 1521-1527.
86. S. K. Ahn, T. Ban, P. Sakthivel, J. W. Lee, Y.-S. Gal, J.-K. Lee, M.-R. Kim and S.-H. Jin, *ACS Applied Materials & Interfaces*, 2012, **4**, 2096-2100.
87. J.-U. Kim, S.-H. Park, H.-J. Choi, W.-K. Lee, J.-K. Lee and M.-R. Kim, *Solar Energy Materials and Solar Cells*, 2009, **93**, 803-807.
88. M. Sethupathy, P. Pandey and P. Manisankar, *Mater.Chem.Phys.*, 2014, **143**, 1191-1198.
89. M. A. K. L. Dissanayake, H. K. D. W. M. N. R. Divarathne, C. A. Thotawatthage, C. B. Dissanayake, G. K. R. Senadeera and B. M. R. Bandara, *Electrochim.Acta*, 2014, **130**, 76-81.
90. P. Joshi, L. Zhang, Q. Chen, D. Galipeau, H. Fong and Q. Qiao, *ACS Applied Materials & Interfaces*, 2010, **2**, 3572-3577.
91. L. Li, P. Zhu, S. Peng, M. Srinivasan, Q. Yan, A. S. Nair, B. Liu and S. Samakrishna, *J. Phys. Chem. C*, 2014, DOI: 10.1021/jp4117529.
92. P. Poudel, L. Zhang, P. Joshi, S. Venkatesan, H. Fong and Q. Qiao, *Nanoscale*, 2012, **4**, 4726-4730.
93. S. Peng, P. Zhu, Y. Wu, S. G. Mhaisalkar and S. Ramakrishna, *RSC Advances*, 2012, **2**, 652-657.
94. S.-H. Park, H.-R. Jung, B.-K. Kim and W.-J. Lee, *Journal of Photochemistry and Photobiology A: Chemistry*, 2012, **246**, 45-49.
95. S. S. Mali, P. S. Patil and C. K. Hong, *ACS Appl. Mater. Interfaces*, 2014, **6**, 1688–1696.
96. J. Kim, J. Kang, U. Jeong, H. Kim and H. Lee, *ACS Appl. Mater. Interfaces*, 2013, **5**, 3176–3181.
97. S.-H. Park, H.-R. Jung and W.-J. Lee, *Electrochim.Acta*, 2013, **102**, 423–428.

98. G. Zhu, L. Pan, J. Yang, X. Liu, H. Sun and Z. Sun, *J.Mater.Chem.*, 2012, **22**, 24326-24329.
99. Y.-F. Wang, K.-N. Li, W.-Q. Wu, Y.-F. Xu, H.-Y. Chen, C.-Y. Su and D.-B. Kuang, *RSC Adv*, 2013, **3**, 13804-13810.
100. H.-Y. Chen, T.-L. Zhang, J. Fan, D.-B. Kuang and C.-Y. Su, *ACS Appl. Mater. Interfaces*, 2013, **5**, 9205–9211.
101. J.-H. Lee, K. Ahn, S. H. Kim, J. M. Kim, S.-Y. Jeong, J.-S. Jin, E. D. Jeong and C.-R. Cho, *Current Appl.Phys.*, 2014, **14**, 856-861.
102. J.-J. Wu, Y.-R. Chen, W.-P. Liao, C.-T. Wu and C.-Y. Chen, *ACS Nano*, 2010, **4**, 5679-5684.
103. P. Zhu, A. S. Nair, S. Yang, S. Peng and S. Ramakrishna, *Journal of Materials Chemistry*, 2011, **21**, 12210-12212.
104. P. Joshi, L. Zhang, D. Davoux, Z. Zhu, D. Galipeau, H. Fong and Q. Qiao, *Energy & Environmental Science*, 2010, **3**, 1507-1510.
105. Y.-L. Chen, Y.-H. Chang, J.-L. Huang, I. Chen and C. Kuo, *The Journal of Physical Chemistry C*, 2012, **116**, 3857-3865.
106. J. Yang, L. Pan, G. Zhu, X. Liu, H. Sun and Z. Sun, *Journal of Electroanalytical Chemistry*, 2012, **677–680**, 101-104.
107. R. A. Naphade, M. Tathavadekar, J. P. Jog, S. Agarkar and S. Ogale, *J.Mater.Chem.A,*, 2014, **2**, 975-984.
108. Y. Horie, M. Deguchi, S. Guo, K. Aoki and T. Nomiyama, *Jpn.J.Appl.Phys*, 2014, **53**, 05FB01.
109. Y. Horie, T. Watanabe, M. Deguchi, D. Asakura and T. Nomiyama, *Electrochim.Acta*, 2013, **105**, 394-402.
110. A. M. Smith and S. Nie, *Acc.Chem.Res.*, 2010, **43**, 190-200.
111. W. A. Tisdale, K. J. Williams, B. A. Timp, D. J. Norris, E. S. Aydil and X.-Y. Zhu, *Science*, 2010, **328**, 1543-1547.
112. M.-J. Jin, T. Ma, T. Ling, S.-Z. Qiao and X.-W. Du, *J.Mater.Chem.*, 2012, **22**, 13057-13063.
113. Y. Shengyuan, A. S. Nair, Z. Peining and S. Ramakrishna, *Materials Letters*, 2012, **76**, 43-46.
114. P. Sudhagar, J. H. Jung, S. Park, Y.-G. Lee, R. Sathyamoorthy, Y. S. Kang and H. Ahn, *Electrochem. Commun.*, 2009, **11**, 2220-2224.
115. P. Sudhagar, V. González-Pedro, I. Mora-Seró, F. Fabregat-Santiago, J. Bisquert and Y. S. Kang, *J.Mater.Chem.*, 2012, **22**, 14228-14235.
116. H. Han, P. Sudhagar, T. Song, Y. Jeon, I. Mora-Seró, F. Fabregat-Santiago, J. Bisquert, Y. S. Kang and U. Paik, *Chem.Commun.*, 2013, **49**, 2810-2812.
117. W. Zhang, R. Zhu, X. Liu, B. Liu and S. Ramakrishna, *Appl.Phys.Lett.*, 2009, **95**, 043304.
118. S. Yun and S. Lim, *Journal of Solid State Chemistry*, 2011, **184**, 273-279.
119. I.-D. Kim, J.-M. Hong, B. H. Lee, D. Y. Kim, E.-K. Jeon, D.-K. Choi and D.-J. Yang, *Appl.Phys.Lett.*, 2007, **91**, 163109.
120. E. N. Kumar, R. Jose, P. S. Archana, C. Vijila, M. M. Yusoff and S. Ramakrishna, *Energy & Environmental Science*, 2012, **5**, 5401-5407.
121. T. Krishnamoorthy, M. Z. Tang, A. Verma, A. S. Nair, D. Pliszka, S. G. Mhaisalkar and S. Ramakrishna, *J.Mater.Chem.*, 2012, **22**, 2166-2172.
122. C. Gao, X. Li, X. Zhu, L. Chen, Z. Zhang, Y. Wang, Z. Zhang, H. Duan and E. Xie, *J.Power Sources*, 2014, **264**, 15-21.
123. N. K. Elumalai, T. M. Jin, V. Chellappan, R. Jose, S. K. Palaniswamy, S. Jayaraman, H. K. Raut and S. Ramakrishna, *ACS Appl. Mater. Interfaces*, 2013, **5**, 9396–9404.
124. N. M. Bedford, M. B. Dickerson, L. F. Drummy, H. Koerner, K. M. Singh, M. C. Vasudev, M. F. Durstock, R. R. Naik and A. J. Steckl, *Adv.Energy Mater.*, 2012, **2**, 1136-1144.
125. J.-Y. Chen, H.-C. Wu, Y.-C. Chiu and W.-C. Chen, *Adv.Energy Mater.*, 2014, DOI: 10.1002/aenm.201301665.
126. S. Wu, J. Li, S.-C. Lo, Q. Tai and F. Yan, *Organic Electronics*, 2012, **13**, 1569–1575.
127. P. S. Kumar, S. A. S. Nizar, J. Sundaramurthy, P. Ragupathy, V. Thavasi, S. G. Mhaisalkar and S. Ramakrishna, *J.Mater.Chem.*, 2011, **21**, 9784-9790.
128. X. Zhang, V. Thavasi, S. G. Mhaisalkar and S. Ramakrishna, *Nanoscale*, 2012, **4**, 1707-1716.
129. P. Du, L. Song, J. Xiong, N. Li, Z. Xi, L. Wang, D. Jin, S. Guo and Y. Yuan, *Electrochimica Acta*, 2012, **78**, 392-397.
130. D. Hwang, S. M. Jo, D. Y. Kim, V. Armel, D. R. MacFarlane and S.-Y. Jang, *ACS Appl. Mater. Interfaces*, 2011, **3**, 1521–1527.
131. B. H. Lee, M. Y. Song, S.-Y. Jang, S. M. Jo, S.-Y. Kwak and D. Y. Kim, *J.Phys.Chem.C*, 2009, **113**, 21453–21457.
132. A. A. Madhavan, S. Kalluri, D. K. Chacko, T. A. Arun, S. Nagarajan, K. R. V. Subramanian, A. S. Nair, S. V. Nair and A. Balakrishnan, *RSC Adv*, 2012, **2**, 13032-13037.
133. S. Yun and S. Lim, *J.Solid State Chem.*, 2011, **184**, 273-279.
134. E. N. Kumar, R. Jose, P. S. Archana, C. Vijila, M. M. Yusoff and S. Ramakrishna, *Energy Environ. Sci.*, 2012, **5**, 5401-5407.
135. Y. P. Lin, S. Y. Lin, Y. C. Lee and Y. W. Chen-Yang, *J.Mater.Chem.A*, 2013, **1**, 9875-9884.
136. P. Zhu, A. S. Nair, S. Yang, S. Peng and S. Ramakrishna, *J.Mater.Chem.*, 2011, **21**, 12210-12212.
137. P. Joshi, L. Zhang, D. Davoux, Z. Zhu, D. Galipeau, H. Fong and Q. Qiao, *Energy Environ. Sci.*, 2010, **3**, 1507-1510.
138. P. Joshi, L. Zhang, Q. Chen, D. Galipeau, H. Fong and Q. Qiao, *ACS Appl. Mater. Interfaces*, 2010, **2**, 3572-3577.
139. S. Peng, P. Zhu, Y. Wu, S. G. Mhaisalkar and S. Ramakrishna, *RSC Adv*, 2012, **2**, 652-657.
140. S.-H. Park, H.-R. Jung, B.-K. Kim and W.-J. Lee, *J.Photochem.Photobiol. A*, 2012, **246**, 45-49.
141. X. Hu, G. Li and J. C. Yu, *Langmuir*, 2010, **26**, 3031–3039.
142. A. D. Paola, E. García-López, G. Marcì and L. Palmisano, *J.Hazard.Mater.*, 2012, **211-212**, 3-29.
143. D. S. Bhatkhande, V. G. Pangarkar and A. A. C. M. Beenackers, *Journal of Chemical Technology & Biotechnology*, 2002, **77**, 102-116.
144. M. R. Hoffmann, S. T. Martin, W. Choi and D. W. Bahnemann, *Chemical Reviews*, 1995, **95**, 69-96.
145. A. L. Linsebigler, G. Lu and J. T. Yates, *Chemical Reviews*, 1995, **95**, 735-758.
146. A. Fujishima and X. Zhang, *Comptes Rendus Chimie*, 2006, **9**, 750-760.
147. A. Kubacka, M. Fernández-García and G. Colón, *Chem.Rev.*, 2011, **112**, 1555–1614.
148. Y. N. Tan, C. L. Wong and A. R. Mohamed, *ISRN Materials Science,*, 2011, **2011**, 18.
149. V. A. Ganesh, A. S. Nair, H. K. Raut, T. M. Walsh and S. Ramakrishna, *RSC Advances*, 2012, **2**, 2067-2072.
150. H. Liu, J. Yang, J. Liang, Y. Huang and C. Tang, *Journal of the American Ceramic Society*, 2008, **91**, 1287-1291.
151. J. Sundaramurthy, P. S. Kumar, M. Kalaivani, V. Thavasi, S. G. Mhaisalkar and S. Ramakrishna, *RSC Advances*, 2012, **2**, 8201-8208.
152. G. Zhao, S. Liu, Q. Lu and L. Song, *Industrial & Engineering Chemistry Research*, 2012, **51**, 10307-10312.
153. V. J. Babu, R. S. R. Bhavatharini and S. Ramakrishna, *RSC Adv.*, 2014, **4**, 19251–19256.
154. J. b. Veluru, R. S. R. Bhavatharini and S. Ramakrishna, *RSC Adv*, 2014, DOI: 10.1039/C1034RA03754E.
155. J. b. Veluru, S. Vempati and S. Ramakrishna, *RSC Adv*, 2014, DOI: 10.1039/C1034RA03498H.
156. J. Mu, B. Chen, M. Zhang, Z. Guo, P. Zhang, Z. Zhang, Y. Sun, C. Shao and Y. Liu, *ACS Appl. Mater. Interfaces*, 2011, **4**, 424-430.
157. D. Mitoraj and H. Kisch, *Angewandte Chemie International Edition*, 2008, **47**, 9975-9978.
158. D. Zhang, G. Li and J. C. Yu, ed. L. Zang, Springer London, 2011, pp. 679-716.
159. J.-Y. Park, K.-J. Hwang, J.-W. Lee and I.-H. Lee, *Journal of Materials Science*, 2011, **46**, 7240-7246.
160. E. Formo, M. S. Yavuz, E. P. Lee, L. Lane and Y. Xia, *Journal of Materials Chemistry*, 2009, **19**, 3878-3882.
161. Z. Zhang, C. Shao, L. Zhang, X. Li and Y. Liu, *J. Colloid Interface Sci.*, 2010, **351**, 57-62.
162. J. Xu, W. Wang, M. Shang, E. Gao, Z. Zhang and J. Ren, *Journal of Hazardous Materials*, 2011, **196**, 426-430.
163. D. Lin, H. Wu, R. Zhang and W. Pan, *Chem. Mater.*, 2009, **21**, 3479-3484.

164. C. H. Kim, B.-H. Kim and K. S. Yang, *Carbon*, 2012, **50**, 2472-2481.
165. L. Li, P. Zhang, R. Liu and S. M. Guo, *J.Power Sources*, 2011, **196**, 1242-1247.
166. P. Zhang, C. Shao, Z. Zhang, M. Zhang, J. Mu, Z. Guo, Y. Sun and Y. Liu, *Journal of Materials Chemistry*, 2011, **21**, 17746-17753.
167. R. Asahi, T. Morikawa, T. Ohwaki, K. Aoki and Y. Taga, *Science*, 2001, **293**, 269-271.
168. Y. Zhang, L. Fei, X. Jiang, C. Pan and Y. Wang, *Journal of the American Ceramic Society*, 2011, **94**, 4157-4161.
169. Y. Wang, J. Zhang, L. Liu, C. Zhu, X. Liu and Q. Su, *Materials Letters*, 2012, **75**, 95-98.
170. R. Liu, H. Ye, X. Xiong and H. Liu, *Materials Chemistry and Physics*, 2010, **121**, 432-439.
171. M. Shang, W. Wang, L. Zhang, S. Sun, L. Wang and L. Zhou, *The Journal of Physical Chemistry C*, 2009, **113**, 14727-14731.
172. Z. Zhang, C. Shao, X. Li, C. Wang, M. Zhang and Y. Liu, *ACS Appl. Mater. Interfaces*, 2010, **2**, 2915-2923.
173. Z. Liu, D. D. Sun, P. Guo and J. O. Leckie, *Nano Letters*, 2006, **7**, 1081-1085.
174. H. Li, W. Zhang, B. Li and W. Pan, *J. Am. Ceram. Soc.*, 2010, **93**, 2503-2506.
175. D. Ma, Y. Xin, M. Gao and J. Wu, *Applied Catalysis B: Environmental*, 2014, **147**, 49-57.
176. C.-J. Li, J.-N. Wang, B. Wang, J. R. Gong and Z. Lin, *Journal of Nanoscience and Nanotechnology*, 2012, **12**, 2496-2502.
177. S. S. Lee, H. Bai, Z. Liu and D. D. Sun, *Water Research*, 2013, **47**, 4059-4073.
178. G. Yang, Q. Zhang, W. Chang and W. Yan, *J. Alloys Compd.*, 2013, **580**, 29-36.
179. X. Peng, A. C. Santulli, E. Sutter and S. S. Wong, *Chemical Science*, 2012, **3**, 1262-1272.
180. I. M. Szilágyi, E. Santala, M. Heikkilä, V. Pore, M. Kemell, T. Nikitin, G. Teucher, T. Firkala, L. Khriachtchev, M. Räsänen, M. Ritala and M. Leskelä, *Chem. Vap. Deposition*, 2013, **19**, 149-155.
181. P. Zhang, C. Shao, X. Li, M. Zhang, X. Zhang, Y. Sun and Y. Liu, *J. Hazard. Mater.*, 2012, **237–238**, 331-338.
182. P. F. Du, L. X. Song, J. Xiong, Z. Q. Xi, J. J. Chen, L. H. Gao and N. Y. Wang, *Journal of Nanoscience and Nanotechnology*, 2011, **11**, 7723-7728.
183. P. Ren, H. Fan and X. Wang, *Catal. Commun.*, 2012, **25**, 32-35.
184. J. Mu, C. Shao, Z. Guo, Z. Zhang, M. Zhang, P. Zhang, B. Chen and Y. Liu, *ACS Appl. Mater. Interfaces*, 2011, **3**, 590-596.
185. Z. Wang, Z. Li, H. Zhang and C. Wang, *Catal. Commun.*, 2009, **11**, 257-260.
186. J. S. Lee, O. S. Kwon and J. Jang, *J. Mater. Chem.*, 2012, **22**, 14565-14572.
187. M. Samadi, H. A. Shivaee, M. Zanetti, A. Pourjavadi and A. Moshfegh, *J. Mol. Catal. A: Chem.*, 2012, **359**, 42-48.
188. C. Li, R. Chen, X. Zhang, S. Shu, J. Xiong, Y. Zheng and W. Dong, *Mater. Lett.*, 2011, **65**, 1327-1330.
189. Y. Liu, H. Yu, S. Zhan, Y. Li, Z. Lv, X. Yang and Y. Yu, *J. Sol-Gel Sci. Technol.*, 2011, **58**, 716-723.
190. S. Zhan, J. Yang, Y. Liu, N. Wang, J. Dai, H. Yu, X. Gao and Y. Li, *J. Colloid Interface Sci.*, 2011, **355**, 328-333.
191. D. Hou, W. Luo, Y. Huang, J. C. Yu and X. Hu, *Nanoscale*, 2013, **5**, 2028-2035.
192. G. Zhao, S. Liu, Q. Lu, M. Shi and L. Song, *J. Cluster Sci.*, 2011, **22**, 621-631.
193. B. Dong, Z. Li, Z. Li, X. Xu, M. Song, W. Zheng, C. Wang, S. S. Al-Deyab and M. El-Newehy, *J. Am. Ceram. Soc.*, 2010, **93**, 3587-3590.
194. X. Wang, H. Fan and P. Ren, *Catal. Commun.*, 2013, **31**, 37-41.
195. V. Štengl, J. Velická, M. Maříková and T. M. Grygar, *ACS Applied Materials & Interfaces*, 2011, **3**, 4014-4023.
196. M. Kanjwal, N. Barakat, F. Sheikh and H. Kim, *Journal of Materials Science*, 2010, **45**, 1272-1279.
197. Z. Zhang, C. Shao, X. Li, L. Zhang, H. Xue, C. Wang and Y. Liu, *The Journal of Physical Chemistry C*, 2010, **114**, 7920-7925.
198. T. Cao, Y. Li, C. Wang, L. Wei, C. Shao and Y. Liu, *Materials Research Bulletin*, 2010, **45**, 1406-1412.
199. M. Jin, X. Zhang, A. V. Emeline, Z. Liu, D. A. Tryk, T. Murakami and A. Fujishima, *Chemical Communications*, 2006, 4483-4485.
200. A. Ma, Y. Wei, Z. Zhou, W. Xu, F. Ren, H. Ma and J. Wang, *Polymer Degradation and Stability*, 2012, **97**, 125-131.
201. A. Yousef, N. A. M. Barakat, T. Amna, A. R. Unnithan, S. S. Al-Deyab and H. Yong Kim, *Journal of Luminescence*, 2012, **132**, 1668-1677.
202. P. V. Kamat, *J.Phys.Chem.C*, 2008, **112**, 18737–18753.
203. N. Han, F. Wang and J. C. Ho, *Insitution of Civil Engineers*, 2011, **http://dx.doi.org/10.1680/nme.11.00005**.
204. E. C. Garnett and P. Yang, *J. Am. Chem. Soc.*, 2008, **130**, 9224–9225.
205. L. Tsakalakos, J. Balch, J. Fronheiser, B. A. Korevaar, O. Sulima and J. Rand, *Appl.Phys.Lett*, 2007, **91**, 233117.
206. A. C. Ford, J. C. Ho, Y.-L. Chueh, Y.-C. Tseng, Z. Fan, J. Guo, J. Bokor and A. Javey, *Nano Lett.*, 2009, **9**, 360-365.
207. K. Takei, T. Takahashi, J. C. Ho, H. Ko, A. G. Gillies, P. W. Leu, R. S. Fearing and A. Javey, *Nature Mater.*, 2010, **9**, 821-826.
208. H. Yan, H. S. Choe, S. W. Nam, Y. Hu, S. Das, J. F. Klemic, J. C. Ellenbogen and C. M. Lieber, *Nature*, 2011, **470**, 240–244.
209. R. Yan, D. Gargas and P. Yang, *Nature Photonics*, 2009, **3**, 569–576.
210. N. S. Lewis, *Science*, 2007, **315**, 798-801.
211. Y.-Z. Long, M. Yu, B. Sun, C.-Z. Gu and Z. Fan, *Chem. Soc. Rev.*, 2012, **41**, 4560–4580.
212. G. Dong, X. Xiao, L. Zhang, Z. Ma, X. Bao, M. Peng, Q. Zhang and J. Qiu, *J.Mater.Chem.*, 2011, **21**, 2194-2203.
213. A. Babel, D. Li, Y. Xia and S. A. Jenekhe, *Macromolecules*, 2005, **38**, 4705–4711.
214. P. Ahmadpoor, A. S. Nateri and V. Motaghitalab, *J.Appl.Polym.Sci*, 2013, **130**, 78-85.
215. L. Gao and C. Li, *J.Luminescence*, 2010, **130**, 236-239.
216. M. M. Munir, F. Iskandar, K. M. Yun, K. Okuyama and M. Abdullah, *Nanotechnology*, 2008, **19**, 145603.
217. J.-Y. Chen, C.-C. Kuo, C.-S. Lai, W.-C. Chen and H.-L. Chen, *Macromolecules*, 2011, **44**, 2883–2892.
218. Y. Shmueli, G. E. Shter, O. Assad, H. Haick, P. Sonntag, P. Ricoux and G. S. Grader, *J. Mater. Res.*, 2012, **27**, 1672-1679.
219. A. Kumar, R. Jose, K. Fujihara, J. Wang and S. Ramakrishna, *Chem. Mater.*, 2007, **19**, 6536–6542.
220. D. Hou, X. Hu, Y. Wen, B. Shan, P. Hu, X. Xiong, Y. Qiao and Y. Huang, *Phys.Chem.Chem.Phys.*, 2013, **15**, 20698-20705.
221. S. Chuangchote, J. Jitputti, T. Sagawa and S. Yoshikawa, *ACS Appl.Mater.Interfaces*, 2009, **1**, 1140-1143.
222. E. C. Garnett, M. L. Brongersma, Y. Cui and M. D. McGehee, *Annu. Rev. Mater. Res.*, 2011, **41**, 269–295.
223. A. I. Hochbaum and P. Yang, *Chem.Rev.*, 2010, **110**, 527-546.
224. B. Tan and Y. Wu, *J.Phys.Chem.B*, 2006, **110**, 15932–15938.
225. Z.-S. Wang, H. Kawauchi, T. Kashima and H. Arakawa, *Coord.Chem.Rev.*, 2004, **248**, 1381-1389.
226. Y.-J. Lee, D. S. Ruby, D. W. Peters, B. B. McKenzie and J. W. P. Hsu, *Nano Lett.*, 2008, **8**, 1501-1505.
227. A. Fujishima and K. Honda, *Nature*, 1972, **238**, 37-38.
228. M. Ni, M. K. H. Leung, D. Y. C. Leung and K. Sumathy, *Renew.Sustain.Energ.Rev*, 2007, **11**, 401-425.
229. M. Ashokkumar, *Int.J.Hydrogen Energy*, 1998, **23**, 427-438.
230. A. Kudo and Y. Miseki, *Chem.Soc.Rev.*, 2009, **38**, 253-278
231. O. Diwald, T. L. Thompson, T. Zubkov, E. G. Goralski, S. D. Walck and J. T. Jr.Yates, *J.Phys.Chem.B*, 2004, **108**, 6004-6008.
232. X. Chen and C. Burda, *J.Phys.Chem.B*, 2004, **108**, 15446-15449.
233. R. Asahi and T. Morikawa, *Chemical Physics*, 2007, **339**, 57-63.

234. T. Ohsawa, I. Lyubinetsky, Y. Du, M. A. Henderson, V. Shutthanandan and a. S. A. Chambers, *Phys.Rev.B*, 2009, **79**, 085401.
235. J. H. Ming-Chung Wu, András Sápi, Anna Avila, William Larsson, Hsueh-Chung Liao, Mika Huuhtanen, Géza Tóth, Andrey Shchukarev, Noémi Laufer, Ákos Kukovecz, Zoltán Kónya, Jyri-Pekka Mikkola, Riitta Keiski, Wei-Fang Su, and H. J. Yang-Fang Chen, Pulickel M Ajayan, Robert Vajtai, and Krisztián Kordás *ACS Nano*, 2011, **5**, 5025-5030.
236. J. B. Varley, A. Janotti and C. G. V. d. Walle, *Adv.Mater*, 2011, **23**, 2343-2347.
237. X. Sun, H. Liu, J. Dong, J. Wei and Y. Zhang, *Catalysis Letters*, 2010, **135**, 219-225.
238. A. Chinnappan and H. Kim, *Int.J.Hydrogen Energy*, 2012, **37**, 18851-18859.
239. S. S. Lee, H. Bai, Z. Liu and D. D. Sun, *Appl.Catal.B*, 2013, **140**, 68-81.
240. J. Jitputti, Y. Suzuki and S. Yoshikawa, *Catal.Commun*, 2008, **9**, 1265-1271.
241. X. Chen, S. Shen, L. Guo and a. S. S. Mao, *Chem.Rev*, 2010, **110**, 6503-6570.
242. H. Bai, Z. Liu and D. D. Sun, *J.Am.Ceram.Soc*, 2013, **96**, 942–949.
243. S. S. Lee, H. Bai, Z. Liu and D. D. Sun, *Int.J.Hydrogen Energy*, 2012, **37**, 10575-10584.
244. Y. Tong, X. Lu, W. Sun, G. Nie, L. Yang and C. Wang, *J.Power Sources*, 2014, **261**, 221-226.
245. K. Maeda, K. Teramura, D. Lu, T. Takata, N. Saito, Y. Inoue and K. Domen, *Nature*, 2006, **440**, 295.
246. X. Chen, C. Li, M. Gratzel, R. Kostecki and S. S. Mao, *Chem.Soc.Rev*, 2012, **41**, 7909-7937.
247. V. J. Babu, M. K. Kumar, R. Murugan, M. M. Khin, R. P. Rao, A. S. Nair and S. Ramakrishna, *Int.J.Hydrogen Energy*, 2013, **38**, 4324-4333.
248. S. K. Choi, S. Kim, J. Ryu, S. K. Limb and H. Park, *Photochem.Photobiol.Sci.*, 2012, **11**, 1437-1444.
249. V. J. Babu, M. K. Kumar, A. S. Nair, T. K. Lee, I. A. Suleyman and S. Ramakrishna, *Int.J.Hydrogen Energy*, 2012, **37**, 8897-8904.
250. L. Macaraig, S. Chuangchote and T. Sagawa, *J.Mater.Res.*, 2014, **29**, 123-130.
251. L. Zhang, J. Kim, E. Dy, S. Ban, K.-c. Tsay, H. Kawai and Z. Shi, *Electrochimica Acta*, 2013, **108**, 480–485.
252. J.-Y. Jhan, Y.-W. Huang, C.-H. Hsu, H. Teng, D. Kuo and P.-L. Kuo, *Energy*, 2013, **53**, 282–287.
253. N. Jha, P. Ramesh, E. Bekyarova, X. Tian, F. Wang, M. E. Itkis and R. C. Haddon, *Scintific Reports*, 2013, **3** 1-7.
254. S. H. Hur and J.-N. Park, *Asia Pacific J. Chemical Eng.*, 2013, **8**, 218–233.
255. R. Kumar, C. Xu and K. Scott, *RSC Adv*, 2012, **2**, 8777–8782.
256. X. Li, W. Cai, J. An, S. Kim, J. Nah, D. Yang, R. Piner, A. Velamakanni, I. Jung, E. Tutuc, S. K. Banerjee, L. Colombo and R. S. Ruoff, *Science*, 2009, **324**, 1312-1314.
257. J. B. Ballengee and P. N. Pintauro, *Macromolecules*, 2011, **44**, 7307–7314.
258. T. Tamura and H. Kawakami, *Nano.Lett.*, 2010, **10**, 1324–1328.
259. W. Li, X. Wang, Z. Chen, M. Waje and Yushan, *Langmuir*, 2005, **21**, 9386–9389.
260. J. M. Kim, H.-I. Joh, S. M. Jo, D. J. Ahn, H. Y. Ha, S.-A. Hong and S.-K. Kim, *Electrochimica Acta*, **55**, 4827-4835.
261. L. Su, W. Jia, A. Schempf, Y. Ding and Y. Lei, *The Journal of Physical Chemistry C*, 2009, **113**, 16174-16180.
262. D. Chen, Y.-E. Miao and T. Liu, *ACS Appl. Mater. Interfaces*, 2013, **5**, 1206–1212.
263. W. J. Kim and J. Y. Chang, *Mater.lett*, 2011, **65**, 1388–1391.
264. N. T. Xuyen, E. J. Ra, H.-Z. Geng, K. K. Kim, K. H. An and Y. H. Lee, *The Journal of Physical Chemistry B*, 2007, **111**, 11350-11353.
265. J.-H. Park, Y.-W. Ju, S.-H. Park, H.-R. Jung, K.-S. Yang and W.-J. Lee, *Journal of Applied Electrochemistry*, 2009, **39**, 1229-1236.
266. M. Li, S. Zhao, G. Han and B. Yang, *Journal of Power Sources*, 2009, **191**, 351-356.
267. M. Li, G. Han and B. Yang, *Electrochemistry Communications*, 2008, **10**, 880-883.
268. Z. Lin, L. Ji and X. Zhang, *Electrochimica Acta*, 2009, **54**, 7042-7047.
269. B. Guo, S. Zhao, G. Han and L. Zhang, *Electrochimica Acta*, 2008, **53**, 5174–5179.
270. N. T. Xuyen, H. K. Jeong, G. Kim, K. P. So, K. H. An and Y. H. Lee, *Journal of Materials Chemistry*, 2009, **19**, 1283-1288.
271. Z. Lin, L. Ji, M. D. Woodroof, Y. Yao, W. Krause and X. Zhang, *J.Phys.Chem.C*, 2010, **114**, 3791–3797.
272. D. Wang, Y. Liu, J. Huang and T. You, *J.Colloid.Interface Sci.*, 2012, **367**, 199-203.
273. L. Su, W. Jia, A. Schempf and Y. Lei, *Electrochemistry Communications*, 2009, **11**, 2199–2202.
274. Z.-G. Zhao, Z.-J. Yao, J. Zhang, R. Zhu, Y. Jin and Q.-W. Li, *J.Mater.Chem.*, 2012, **22**, 16514-16519
275. E. Formo, Z. Peng, E. Lee, X. Lu, H. Yang and Y. Xia, *J. Phys. Chem. C*, 2008, **112**, 9970–9975.
276. Z. Lin, L. Ji, O. Toprakci, W. Krause and X. Zhang, *Journal of Materials Research*, **25**, 1329-1335.
277. S. K. Nataraj, B. H. Kim, J. H. Yun, D. H. Lee, T. M. Aminabhavi and K. S. Yang, *Synthetic Met.*, 2009, **159**, 1496–1504.
278. C. Tekmen, Y. Tsunekawa and H. Nakanishi, *J.Mater. Process Technol.*, 2010, **210**, 451-455.
279. N. Seki, T. Arai, Y. Suzuki and H. Kawakami, *Polymer*, 2012, **53**, 2062-2067.
280. Y. Chang, G. Han, M. Li and F. Gao, *Carbon*, 2011, **49**, 5158-5165.
281. S. Chen, G. He, A. A. Carmona-Martinez, S. Agarwal, A. Greiner, H. Hou and U. Schröder, *Electrochem. Commun.*, 2011, **13**, 1026-1029.
282. S. Chen, H. Hou, F. Harnisch, S. A. Patil, A. A. Carmona-Martinez, S. Agarwal, Y. Zhang, S. Sinha-Ray, A. L. Yarin, A. Greiner and U. Schröder, *Energy Environ. Sci.*, 2011, **4**, 1417-1421
283. M. Ghasemi, S. Shahgaldi, M. Ismail, B. H. Kim, Z. Yaakob and W. R. W. Daud, *Int. J. Hydrogen Energy*, 2011, **36**, 13746-13752.
284. Y. Zhang and A. L. Yarin, *Langmuir*, 2011, **27**, 14627–14631.
285. Y. Ding, W. Jia, H. Zhang, B. Li, Z. Gu and Y. Lei, *Electroanalysis*, 2010, **22**, 1911-1917.
286. P. Schechner, E. Kroll, E. Bubis, S. Chervinsky and E. Zussman, *Journal of The Electrochemical Society*, 2007, **154**, B942-B948.
287. J. Choi, K. M. Lee, R. Wycisk, P. N. Pintauro and P. T. Mather, *J. Electrochem.Soc*, 2010, **157**, B914-B919.
288. M. Zhi, S. Lee, N. Miller, N. H. Menzler and N. Wu, *Energy Environ. Sci.*, 2012, **5**, 7066-7071
289. N. T. Hieu, J. Park and B. Tae, *J. Mater.Sci.Eng.B*, 2012, **177**, 205-209.
290. A. M. Al-Enizi, A. A. Elzatahry, A.-R. I. Soliman and S. S. Al-Theyab, *Int. J.Electrochem.Sci.*, 2012, **7**, 12646 - 12655.
291. S. Martwiset and K. Jaroensuk, *J. Appl.Poly.Sci.*, 2012, **124**, 2594–2600.
292. J. Choi, K. M. Lee, R. Wycisk, P. N. Pintauro and P. T. Mather, *J.Mater.Chem.*, 2010, **20**, 6282-6290
293. C. Alessandra, S. Ada, B. Concetta, F. Patrizia, A. P. Luigi and P. Enza, *J.Nanosci.Nanotechnol.*, 2011, **11**, 8768-8774.
294. R. Bajon, S. Balaji and S. M. Guo, *Journal of Fuel Cell Science and Technology*, 2009, **6**, 031004-031004.
295. J. B. Ballengee and P. N. Pintauro, *J. Electrochem. Soc.*, 2011, **158**, B568-B572.
296. I. Shabani, M. M. Hasani-Sadrabadi, V. Haddadi-Asl and M. Soleimani, *J.Membrane Sci.*, 2011, **368**, 233-240.
297. M. M. Hasani-Sadrabadi, I. Shabani, M. Soleimani and H. Moaddel, *J.Power Sources*, 2011, **196**, 4599-4603.
298. S. W. Choi, Y. Z. Fu, Y. R. Ahn, S. M. Jo and A. Manthiram, *Journal of Power Sources*, 2008, **180**, 167-171.
299. T. Tamura, R. Takemori and H. Kawakami, *Journal of Power Sources*, **217**, 135-141.

300. S. Subianto, S. Cavaliere, D. J. Jones and J. Rozière, *J. Poly.Sci. A: Poly.Chem.*, 2013, **51**, 118-128.
301. W. Liu, S. Wang, M. Xiao, D. Han and Y. Meng, *Chem. Commun*, 2012, **48**, 3415-3417.
302. Y. Yao, Z. Lin, Y. Li, M. Alcoutlabi, H. Hamouda and X. Zhang, *Adv.Energy Mater.*, 2011, **1**, 1133-1140.
303. Y. Yao, L. Ji, Z. Lin, Y. Li, M. Alcoutlabi, H. Hamouda and X. Zhang, *ACS Appl. Mater. Interfaces*, 2011, **3**, 3732–3737.

Graphical Abstract

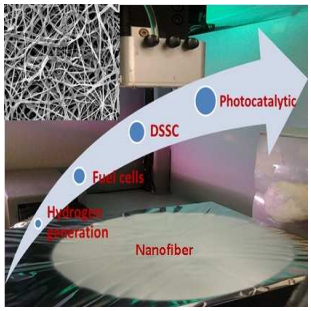

Recent developments in synthesis of electrospun nanomaterials and its potential prospects in energy and environmental applications are discussed in detail.

Broader context

In recent years, the world has been facing enormous challenges such as energy demand, depleting power sources, and environmental pollution. In order to overcome these challenges, much attention has been focused to create new hierarchical nanostructured materials and technology to adopt for cleaner solutions and renewable sources of energy. Although, various methods such as precipitation, hydrothermal, sol-gel have been adapted to synthesis novel nanostructures, electrospinning is one of the simplest and most effective technologies with scale-up potential for wide range of nanomaterials towards industrial production. This review highlights the recent developments in fabrication of one dimensional nanostructured fibers from metals, metal oxides, carbon nanofibers, nanocomposite materials and so on using electrospinning technique. These electrospun nanomaterials exhibited enhancement in performance compared to conventional materials. In this review, we attempt to provide a detailed overview of such nanostructured materials in specific applications such as photovoltaics, photocatalysis, hydrogen generation and fuel cells. We believe that this review will provide sufficient background information and knowledge about electrospinning and pave the way for new innovations of electrospun nanomaterials in energy and environmental applications.